The effect of aviation anti-wear additives on tribofilm formation and micropitting propensity

Airey, Jake; Simpson, James; Spencer, Matthew; Greenwood, Richard W; Simmons, Mark

The Effect of Aviation Anti-Wear Additives on Tribofilm Formation and Micropitting Propensity

Jake Airey [a,b], James Simpson [b], Matthew Spencer [a], Richard W. Greenwood [b], Stuart Blackburn [b], Mark J. H. Simmons [b]

a Rolls-Royce plc, PO Box 31, Derby, DE24 8BJ, UK

b School of Chemical Engineering, University of Birmingham, Edgbaston, B15 2TT, UK

1 Abstract

Micropitting is a prevalent rolling contact fatigue (RCF) wear mechanism which is commonly found on the dedenda in gear contacts and has been shown to be heavily influenced by anti-wear additive chemistry. This article studies the effect of different anti-wear additives on micropitting propensity and tribofilm formation. In particular, anti-wear additives used in aviation applications have been compared against a commonly used automotive anti-wear additive (Zinc Dialkyl Dithio Phosphate ((ZDDP)) that is known to promote micropitting. All of the tests were performed under test conditions representative of the new Power GearBox (PGB) within Rolls-Royce's new engine; the UltraFan©. Tests using a micropitting rig (MPR) found that ZDDP formed micropits at the fastest rate, which then propagated onto the largest amount of wear showing the catastrophic effects of micropitting. Whereas the other aviation anti-wear additives; TriCresyl Phosphate (TCP) and Additive X, formed micropits at a slower rate, but still faster than the formulation without additives containing only base oil. Focus Variation Microscopy (FVM) was used to characterise the micropits and found that ZDDP formed smaller and shallower micropits than the other additives which were comparable and as a result, the wear track of the ZDDP roller had the lowest roughness. Tests on the base oil alone showed a slower generation of micropits, which propagated quickly a more severe failure mode showing the harmful effects of having no anti-wear additive present. Talysurf results showed the counterface ring roughness for ZDDP remained the highest, confirming the literature mechanism that ZDDP forms a tribofilm quickly. This protects asperities which consequently promote micropitting, as high localised asperity contact pressures are maintained. This was further confirmed by evaluating the tribofilms using a Mini Traction Machine with Spacer Layer IMaging (MTM-SLIM) to form tribofilms under representative conditions. This demonstrated that ZDDP forms a thicker tribofilm than the aviation anti-additives and at a faster rate. Overall, the study showed that the aviation anti-wear additives promote micropitting less than

ZDDP, but more that base oil alone. The slower action of the tribofilm formation allows the initial running-in on the tribological contacts, which therefore slows down the initiation of micropitting.

2 Introduction

Modern aviation lubricants have evolved from mineral oil-based to entirely synthetic compounds. Whilst improving thermal stability, this change resulted in a decrease in tribological performance as mineral oils often contained a variety of naturally occurring sulphur species, which impart some wear protection. These species, not separated out due to cost, contributed to enhancing performance without the need for further purification[1,2]. As gas turbine technology progressed and turbine temperatures increased to improve overall efficiency, there was a need for superior high temperature stability, which subsequently led to the use of synthetic group V polyol esters base oils [3]. Consequently, the natural tribological properties imparted from the crude oil were now absent and additives were used to give the required wear protection. Anti-wear additives have become an essential component of most lubricant formulations, as they are vital in ensuring protection under extreme pressure, boundary and mixed lubrication regimes due to their ability to improve load carrying capacity and provide a protective tribofilm onto machine components.

Anti-wear additives are used to reduce wear by protecting surface asperities when the fluid lubricant film is not thick enough to separate opposing asperities, where asperities are defined as the microscopic protruding parts of a surface that contact an opposing surface. Boundary lubrication can be broken down into categories depending on their temperature and load, in a gas turbine oil system these are classified as high temperature and high-pressure contacts. The mechanism of boundary lubrication involves a chemical reaction between the anti-wear additives and the metal surface to create a chemisorbed tribofilm that serves as a constantly replenished sacrificial film that is preferentially sheared off instead of the substrate metal [1,4].

These additives are vital to the performance of the lubricant as the oil system will operate across a variety of lubrication regimes during a flight cycle including cold starts, cruise and landing. Therefore, as these surfaces may be moving slower, this means the lubricant fluid film thickness is insufficient to protect surface asperities and therefore, relies on anti-wear additives to mitigate wear.

Whilst anti-wear additives are known to be proficient in protecting against wear, their effect on less severe wear mechanisms such as micropitting, which is a common wear mechanism seen in gear environments, has been less studied. This paper focuses on the influence of different anti-wear additives on micropitting. This is motivated by the development of the new Power Gear Box (PGB) in Rolls-Royce's new engine; the UltraFan©, as it needs to be understood whether current lubricants can adequately protect this new tribological environment. The PGB will incorporate extremely high loads

in order to drive efficiency, but this results new highly loaded tribological contact unlike any other contact already in the aviation transmission system.

Micropitting has been shown to be influenced by a wide range of different parameters including load, roughness, SRR, the speed of the surfaces, the hardness, the temperature and type of lubricant and additives present in the formulation as summarised by Laine *et al.* [5]. It has also been found that the fluid pressure in the contact also contributes to opening the crack, accelerating micropitting [6,7].

They found that the above parameters influenced micropitting in the following ways [8,9,18–21,10–17]:

- Micropitting could be reduced or prevented by increasing the lambda ratio by decreasing the surface roughness (by superfinishing for example) or by increasing the fluid film thickness through controlling the test conditions or controlling the viscosity of the lubricant.
- Increasing the Slide-Roll Ratio (SRR) reduces the micropitting initiation life, but has limited effect on the wear rate [10].
- Not having a differential hardness between meshing components. Softer surfaces are more susceptible to micropitting which, is why Micropitting Rig (MPR, used in this paper) test specimens are designed to have a softer roller specimen in comparison to the counterface rings[10].
- The slower moving component is more likely to be micropitted.
- Certain anti-wear additives have been shown to promote micropitting [14,16,19,20].

Some anti-wear additives are known to promote micropitting [5,14,16,19,20,22]. In particular, many of these studies have observed the effect of one of the most common anti-wear additives mainly used in the automotive industry; zinc dialkyl dithiophosphate (ZDDP), Figure 4. However, aerospace lubricants prohibit the use of additives such as ZDDP due to poor temperature stability, which, would lead to the formation of toxic and corrosive species. These include hydrogen sulphide, mercaptans and olefins. Metal containing additives can cause corrosion problems due to the catalytic nature of metals promoting lubricant breakdown. Consequently, aerospace lubricants use "ashless" anti-wear additives (metal free additives) that are more temperature stable. The most common aviation anti-wear additive is Tri Cresyl Phosphate (TCP), Figure 4, and is usually added in concentrations of ~1-3% in the lubricant formulation [1]. This is an effective anti-wear additive, but forms much thinner tribofilms than ZDDP and therefore, generally provides less wear protection [23]. It has been found in the literature that ZDDP tribofilms stabilise at a thickness of approximately 120 nm and TCP films tend to form additive films around 30 nm thick [23,24]. However, it is more stable at the higher temperatures experienced within a gas turbine oil system [1]. It has been frequently observed that TCP forms a coloured film on the surface of the metal and this film has been attributed to the reduction of wear and friction in the boundary lubrication regime [25–28].

However, there have been limited studies that have investigated whether ashless additives like TCP also influence micropitting [29,30]. Trivedi et al. demonstrated that TCP actually had a positive effect on rolling contact fatigue (RCF) life, however, these tests were done on a ball on rod rig, with a 3 cSt formulation, contact pressure of 5.5 GPa, lambda 0.04 on a range of bearing steels [31]. Although this suggests TCP may not promote micropitting like ZDDP, this study used different conditions to the PGB gear conditions in this paper. Therefore, it needs to be understood whether ashless anti-wear additives used in aviation lubricants like TCP also promote micropitting as this could be a potential failure mode for the PGB.

To evaluate the performance of anti-wear additives, it is important to understand the mechanism by which, they chemically react with the surface to form a tribofilm, but also to understand what the mechanical drivers are for tribofilm formation and growth. It is well known that ZDDP forms relatively thick tribofilms that have a rough and patchy topography, often being described as "pad-like" as confirmed by Atomic Force Microscopy and SLIM [32–39]. It has also been noted this patchy thick film comprises of a multilayer film of iron phosphate and iron sulphide, followed by sulphide in the bulk and then topped off with a zinc sulphide and organic sulphide on the top [30,40]. TCP films are usually only described as being thin in comparison to the likes of ZDDP and therefore, do not incur any notable morphological features that have the same effect as the ZDDP tribofilm [23,30,41].

The mechanism of ZDDP tribofilm formation has been extensively studied, however, it was only recently found that the ZDDP tribofilm does not need solid asperity-asperity contact to drive its formation [42,43]. This was found by conducting a test with a high-EHD friction fluid and no asperity contact using an MTM-SLIM, and it was found that a ZDDP tribofilm still formed. The applied shear stress was sufficient to reduce the thermal activation energy to initiate film formation. Consequently, it confirmed that sliding is required for tribofilm formation as it generates the applied shear stress, which, is absent in pure rolling conditions. This proposed mechanism explains many of the tribological behaviours produced from ZDDP, including the rough pad like topography and morphology of ZDDP. Tribofilm formation will occur at the asperity conjunctions where the contact pressure and, therefore, the shear stress is the highest. The tribofilm will continue to grow at these locations, as they will bear the majority of the load. This will result in deep valleys in between the pads where minimal tribofilm will grow as there is negligible shear stress in those areas [32,42,44]. It has been shown in many studies that ZDDP tribofilms form rapidly and then level out at a maximum tribofilm thickness [32–37]. This levelling out was suggested to be due to the phosphate-glass tribofilm plastically deforming, which, increases the contact area such that the shear stress decreases and eventually reached a point where it is too low to further drive tribofilm growth [42]. It was previously believed that an equilibrium was eventually reached where the rate of tribofilm formation equalled the rate of removal. However, Fujita et al. [34,45]

demonstrated that there was no ZDDP tribofilm loss after a tribofilm was produced and then the lubricant was replaced with base oil for the remainder of the test.

ZDDP tribofilm formation is not highly dependent on the surface material as long as the surfaces have a high hardness and elastic moduli to sustain the applied shear stress. There may be some chemical surface influence to promote the initial adhesion ZDDP to the surface, but the mechanism of growth of the ZDDP tribofilm is believed to be an oligomerisation process [46].

However, the mechanochemical mechanism has been proven for ZDDP and shows a clear driver behind film formation which, is potentially transferrable to ashless additives too. However, the slower formation and thinner thickness of these tribofilms further increases the difficulty in understanding their formation, composition and mechanical properties.

The mechanism of TCP tribofilm formation is less understood but there have been a few theories suggested supported by experimental evidence which have been reviewed by Guan et al. 2015 [41]. Most suggest the formation of a "phosphate glass" tribofilm similar to that from ZDDP, but Guan et al. 2015 reviewed a range of mechanisms from mechanochemical and thermal promoted reactions to others like metal catalysed formation. Hence, the mechanism behind TC tribofilm formation is less conclusive than ZDDP most likely due to it being studied less, but, also due to the increased difficulty in studying a tribofilm that forms slowly and is thinner.

ZDDP has been shown to promote micropitting in comparison to base oils [5,14,22,47,48]. The mechanism by which, this is believed to occur is that the additive prevents initial smoothening of components as they "run-in" by protecting asperities too early, thereby, maintaining many high asperity contact pressures which, encourages micropitting [5,14,22,47,48].

This mechanism was investigated by Ueda et al. [22] using an optical interferometry technique on a ball on disc tribometer that allowed the in-situ measurement of the thickness of a tribofilm (MTM-SLIM, also used in this study). This technique monitored tribofilm formation and noted that film formation coincided with an increase in friction which, was attributed to both the patchy morphology of the ZDDP tribofilm, and also the maintained surface roughness as asperities were protected and prevented from running in. It was also found that that the ZDDP tribofilm formation reached a steady state where the friction remained constant and the thickness of the tribofilm remained constant, which, could potentially indicate the rate of formation and removal of the tribofilm had reached a steady state[30,38,39]. However, this could now be due to the plastic deformation of the phosphate glass tribofilm leading to an increased contract area which could decrease the shear stress below the minimum required to drive tribofilm formation [38,43]. It has also been found that by adding the ZDDP after the initial running in of components completely mitigates the accelerated micropitting seen previously [49,50].

This paper explores the effect of different additives on micropitting using a MPR to observe the progression of micropitting on ….??? from different additives and with different concentrations. An MTM-SLIM was also used to understand the tribofilms produced by the additives at different concentrations in order to provide fundamental understanding of how these tribofilms contributed to the micropitting seen from different additives.
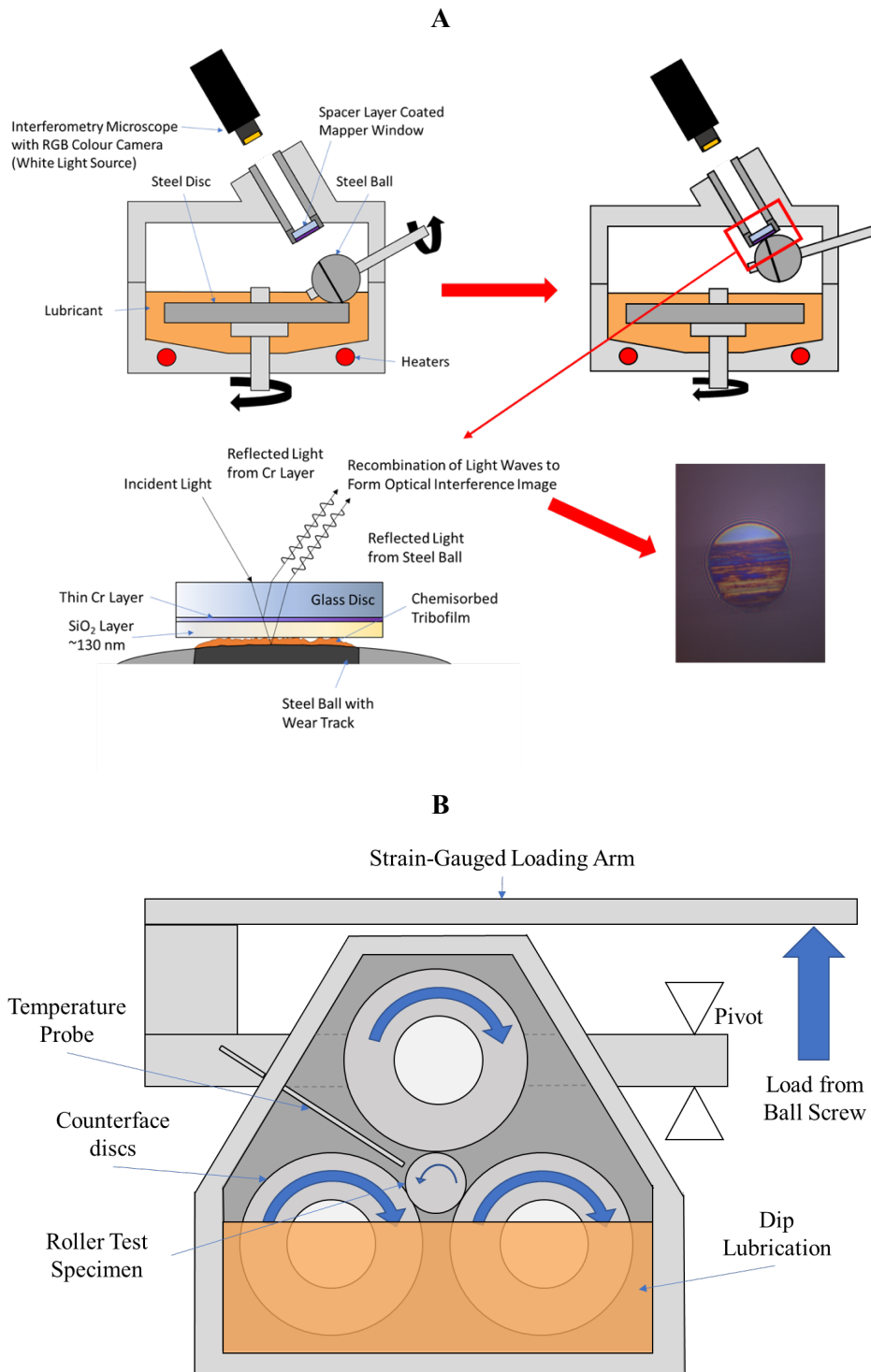
3 Experimental

Figure 1 – A shows a schematic demonstrating the functionality of the MTM-SLIM technique and B shows a diagram illustrating the layout of the MPR showing how the rings and roller rotate and how the load is exerted on the roller specimen.

3.1 Micropitting Rig

Micropitting experiments were conducted using a Micropitting Rig (MPR) developed by PCS instruments. The MPR, shown in Figure 1, is a rolling contact fatigue rig that measures friction under a range of sliding and rolling conditions under lubrication. The contact geometry incorporates a central roller surrounded by three counter-face rings spaced 120 ° apart. Equal loads are applied at each of the three contact points and the contact geometries are line contacts. The load is applied via a stepper motor driven ball-screw which, transfers the load via the load beam to the top counter-face ring. Both the disc and roller specimens are driven by independent electric motors which, enables a range of SRR to be achieved and the assembly is dip lubricated from a temperature-controlled oil sump which, allows a smaller quantity of oil to be used for each test.

This rig can be used to assess lubricant performance by simulating lifetime wear and allows observation of micropitting progression. This rig allows the central roller to be taken out in between tests to enable observation and measurements of the roller to be acquired. Having three rings in contact with the roller allows accelerated testing due to the use of the three rings tripling the amount of contact cycles within a certain time.

The load, the rotational speed of the rollers and rings, the lubricant temperature and the SRR can be controlled. A variety of outputs are measured such as the acceleration signal (essentially a measure of vibration), the friction/ traction coefficient, the wear and the torque.

It should be noted that the exact conditions in used in the PGB cannot be disclosed for Intellectual Property (IP) reasons, but are considered representative of a line contact within the meshing of the gears in that environment. Test conditions were chosen to evaluate lubricant performance under representative PGB conditions, but also used boundary regime to promote micropitting formation and initiate boundary additive reactions with the surface. This test procedure was completed twice for each lubricant.

The conditions are representative worst case conditions expected during operation of the PGB. However, due to the range of speeds, temperatures and variation in the meshing of the gear teeth during different parts of the engine cycle, the gears will undergo a range of tribological environments. A gear tooth typically experiences a range of SRR throughout the process of the gear teeth meshing together due to certain in contact points rolling over one another and other points sliding across the opposing surface. The test followed a series of constant speed wear steps shown in Table 1 and the conditions are shown in Table 2. A series of wear steps allows intermittent observation of the central roller using optical microscopy and an oil change was done after the first step to remove any initial wear metal generated from running in the specimens to prevent other wear mechanisms not caused directly by the oil formulation. Previous studies have shown that wear debris can lead to other surface initiated fatigue

mechanisms and third body abrasive wear in the EHD and boundary regimes. Sayles and Macpherson [51] found a sevenfold increase in L_{10} bearing life and a result of changing the filter size from 40 μm to 3 μm. L_{10} bearing life is the number of cycles that a 90% group of apparently identical bearings will complete prior to the initiation of fatigue and therefore, 10 % of the bearings are not expected to achieve the L_{10} life. Presence of more larger debris was found to lead to debris indentations on the contacting surfaces and which, create new fatigue initiation sites [51]. Nikas et al. (22) also showed that wear debris can also be responsible for scuffing caused by agglomeration of wear debris in the inlet of the EHD contact area and localised melting as a result of the heat created from friction of sliding wear debris [52].

Table 1 - The steps in the MPR test describing when the oil is changed and the duration of each step.

Step	Oil	Number of Contact Cycles	Time of Step (Hr:min:sec)
1	Fresh Oil	73,000	00:05:07
1'	No change	Stribeck Curve	n/a
2	Change Oil	440,000	00:30:48
3	No Change	880,000	01:01:35
4	No Change	1,320,000	01:32:23
5	No Change	1,760,000	02:03:11
6	No Change	2,200,000	02:33:58
7	No Change	2,640,000	03:04:46
8	No Change	3,080,000	03:35:34
9	No Change	3,520,000	04:06:21
10	No Change	3,960,000	04:37:09
11	No Change	4,400,000	05:07:57
11'	No Change	Stribeck Curve	n/a

Table 2 – Table showing the MPR test conditions.

Parameter	Value
Load	165 N
Contact Pressure	1.1 GPa
Lambda Ratio	0.09
SRR	10 %
Entrainment Speed	3.15 m/s
Average PGB Bulk Oil Temperature	100 °C

The accuracy of this calculation was improved by using Jaegers theory of moving hotspots to calculate the inlet temperature between the ring and roller and then the Walther equation (used in ASTM D341) was used to calculate the exact viscosity in the contact by accounting for this temperature increase in the contact [53,54]. These equations can be seen in the appendix section 10.1. Stribeck curves

were also completed at the beginning and end of the test again to look for changes due to differences in the specimens due to wear and due to changes in the lubricant. The Stribeck curves also used the same conditions shown in Table 2 except the entrainment speed was varied from 0 m/s to 3.5 m/s. Tests have shown that the base oils tested are Newtonian up to shear rates of 200 s^{-1} due to the measurement limitation of the cone and plate rheometer ejecting the low viscosity fluid samples due to centrifugal forces at high shear rates. It is assumed that these base oils are all Newtonian in the EHD regime as well as shown by Moore (1997) [55].

To quantify the amount of micropitting on the surface of the MPR roller specimens, a method was developed using the image analysis freeware ImageJ. This can be seen in Figure 2.
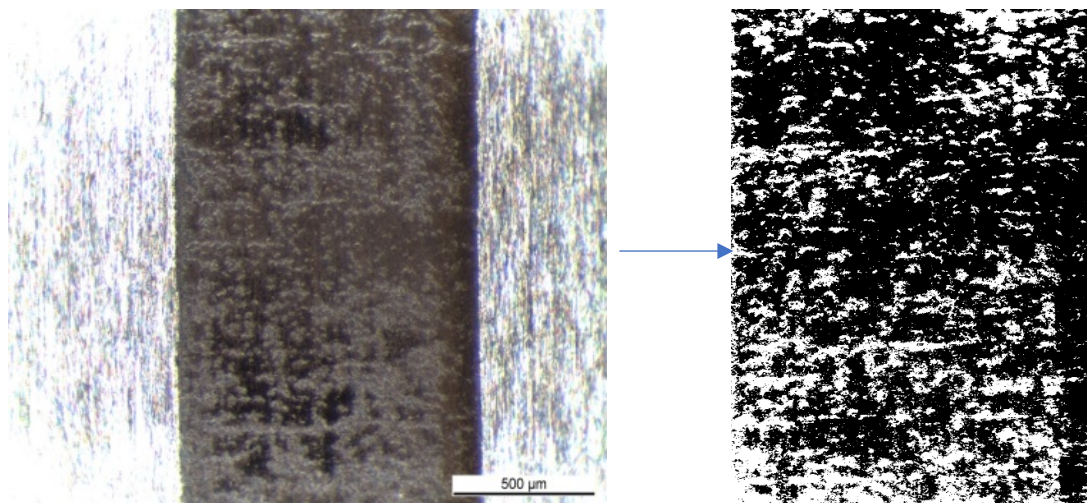

Figure 2 - Image showing how an optical microscope image was converted to allow quantification of micropitting.

This method involved converting the optical microscope image to the greyscale, cropping the image leave just the wear track and then applying a binary threshold. Particle analysis can then be applied to count the amount of micropits which, have been converted into white areas and a percentage micropitted area was also deduced. For this method, images taken after step 2 were selected in order to conduct the image analysis on a "cleaner" micropitted surface before the surfaces become too damaged with extensive wear.

Roughness measurements on MPR Specimens were performed using a Form Talysurf Series 2 profilometer made by Taylor-Hobson which, measures roughness by detecting the deflection of a pin which, is being rastered across a surface. Wear tracks on both the roller and rings were measured in four places and a mean average was taken. The cut-off wavelength was 0.25 mm, data length was 3 mm and the filter was Gaussian.

3.2 Mini Traction Machine with Spacer Layer Imaging

A Mini Traction Machine with Spacer Layer Imaging (MTM-SLIM, developed by PCS instruments) was used to evaluate the tribological performance of the oils. The MTM-SLIM performs a wear test that uses a ball on a disc configuration, each component with a separately controlled rotational speed (and therefore, entrainment speed (U)) to achieve the defined slide-roll ratio (SRR). The contact between the ball and the disc is submerged in a reservoir of lubricant (approximately 35 mL) and the ball rotates against the disc at an inclined axis to eliminate spin in the contact. The load and lubricant temperature can also be controlled and the traction coefficient (friction) is measured. Under normal operation of the MTM the ball rotates anti-clockwise and the disc rotates. Whilst the MTM physically conducts the wear test between the test specimens, the SLIM uses optical interferometry to measure the thickness and topography of boundary additive films that form within the contact of the moving surfaces. A schematic showing how the MTM-SLIM works can be seen in Figure 1. After a defined wear test interval, the ball specimen periodically lifts off the disc and contacts the mapper window of the interferometric microscope with the wear track on the ball specimen. An interferometric image is then taken of the Hertzian contact which, produces an image where the colours can be interpreted as a tribofilm thickness using the film thickness/ colour calibration that is pre-set in the instrument. Other instruments utilise similar SLIM technology to measure the lubricant film thickness in the EHD regime. However, in these experiments, this technique has been applied to a stationary ball to find the boundary additive thickness rather than the full fluid lubricant film separating the two moving surfaces. Further details about the fundamentals of the SLIM apparatus and the principles of interferometry have been published [56,57].

The test consists of a series of constant speed and SRR wear steps, Stribeck curve steps and interferometric imaging steps. This occurs in-situ without any rinsing or cooling of the ball as it has been shown that the action of the ball contacting the window squeezes out any residual oil leaving only the chemisorbed tribofilm [56]. The wear test uses a fixed, slow entrainment speed of 35 mm s^{-1} to ensure that the test operates in the boundary to mixed lubrication regimes to ensure asperity contact, giving rise to the contact conditions necessary to initiate boundary film formation. The additive type is expected to have negligible impact on the lambda ratio due to the viscometric behaviour and pressure-viscosity coefficient being influenced mostly by the base oil.

Prior to the start-up of each test, the test specimens were cleaned to remove their protective anti-corrosive coating which, is applied by the manufacturer for protection and preservation of the specimens. They were cleaned by consecutive immersion in an ultrasonic bath with acetone for 10 minutes and then for a further 10 minutes in petroleum ether. Each test was performed using fresh unworn specimens and at the end of the test the specimens were cleaned with petroleum ether in an ultrasonic bath for 10 minutes and then stored in a sealed plastic wallet to preserve the tribofilm build-up and thus allow further surface analysis to be done.

As well as conducting wear tests at constant entrainment speeds and SRRs, Stribeck tests were also performed throughout the procedure. Seven Stribeck curves were recorded for each test which, allows the variation over time to be observed. The conditions for the Stribeck curve (constant SRR and varying entrainment speed) are shown in Table 3.

Table 3 – SLIM wear test conditions.

Parameter	Value
Load (N)	35
Contact Pressure* (GPa)	0.96
Lambda Ratio	0.11
Window Load (N)	20
Wear test entrainment speed (mm/s)	35
Test Duration (h)	12
Temperature (°C)	100
SRR (%)	100
Stribeck Intervals	Every 2 hours
SRR for Stribeck Curves	50
Entrainment Speed range for Stribeck curves (mm/s)	0 – 3000

* Calculated using the Hertzian contact pressure calculation for a point contact.

To plot the Stribeck curves the traction coefficient was plotted against the Hersey number ($\mu N/p_0$, where N is the entrainment speed in revolutions per second, μ is the dynamic viscosity and p_0 is the maximum contact pressure) to normalise for viscosity. The dynamic viscosities were calculated using the supplied densities and can be seen in section **10.4** in the Appendix.

3.3 Focus Variation Microscopy

To further characterise the produced micropitting, the samples were examined with focus variation microscopy (FVM). FVM is a technique in which a reflective optical microscope scans vertically above a sample surface whilst capturing images. The contrast of the images is then analysed in order to determine the height at which a given lateral position is most in focus [58]. Each lateral position with its assigned height value is combined to produce a 3D dataset. By translating the sample surface laterally, multiple such datasets can be captured and combined to form a dataset that is larger than the field of view of the chosen objective.

In this study, a Bruker Alicona InfiniteFocusG5 was used to acquire 3D scans of the surface of wear track specimens. Scan areas of approximately 1x4 mm were acquired using the x50 magnification objective, which yielded scans with a lateral resolution of 2.135 μm and a vertical resolution of 0.104 nm. Each dataset comprised 270 individual scans and took around 25 minutes to capture. Instrument parameters of exposure 30 μs, gain 0.4, and repeatability threshold 0.06 μm were used to obtain the scans. These settings were deemed acceptable as they produced near complete scans with all points above the repeatability threshold for almost all specimens.

After capturing the dataset, each scan was subjected to several post-processing steps as outlined in Figure 3. Form removal was carried out in the Alicona MeasureSuite software by fitting a cylinder to the as-captured scan. L filtering was then carried out on the form removed surface with a nesting index of 250 µm with an ISO 16610-71 robust gaussian filter for planar surfaces. The robust filter was found to be particularly effective in removing waviness and maintaining the form of the pits in comparison to a regular gaussian filter which resulted in filtering artefacts at the rim of pits. This value was used for the L filter as it was observed to remove the waviness of the wear sample without affecting roughness and pitting. Finally, a reference plane was fit to the form-removed and L-filtered surface by least squares regression.

A real surface roughness and bearing area curve measurements were calculated in the MeasureSuite software package on 250x250 µm square sections of the full scans. Pit characterisation was carried out in MATLAB. The imported scans were binarized into pit or surface with a qualifying depth of 2.5 µm relative to the reference plane. Pit depth was taken as the distance between the reference plane and the minimum data point in the pit. Pit area is calculated from the projected pit area and volume was calculated using the MATLAB boundary function.

It should be noted that these roller specimens were analysed following step 11 of the test regime unlike what was done for the image J analysis. It is recognised that analysing earlier in the test profile would have potentially given simpler surfaces to analyse with less damage and it would advantageous to do this in future.
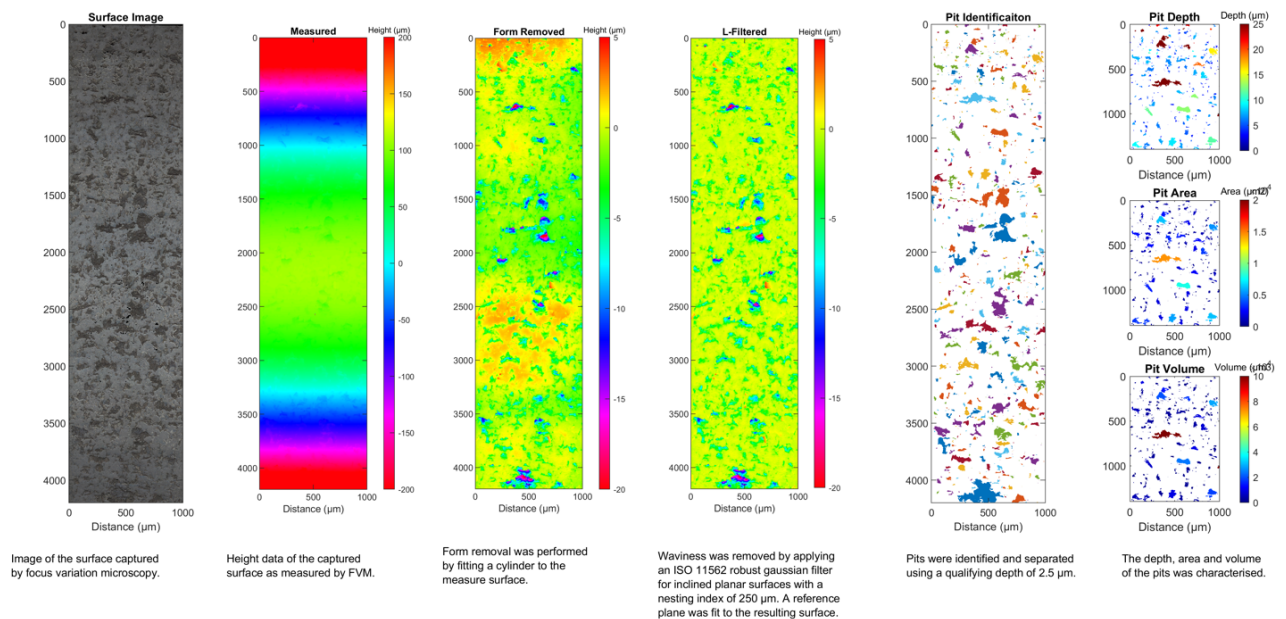

Figure 3 – Schematic illustration how FVM is using to capture an image of the micropitted wear track and how the post processing implemented enables micropitting analysis and characterisation.

13

3.4   Lubricants Tested

. Three different anti-wear additives were tested over a range of concentrations in a standard base oil package used in a commercially available aviation lubricant. The additives are ZDDP, TCP and another ashless phosphorus-based additive called "Additive X" (the details cannot be shared as it is commercially sensitive). The molecular structures of ZDDP and TCP can be seen in Figure 4. A summary of the test oils can be seen in Table 4.

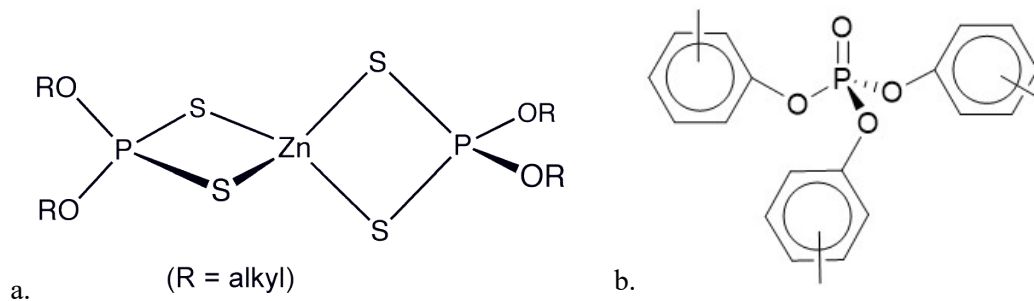a.   (R = alkyl)   b.

Figure 4 - Anti-wear additives; a. ZDDP and b. TCP.

Table 4 – Table showing the test blends with different concentrations of different anti-wear additives.

Oils for Anti-wear Additive Study
Pure Base oil
800 ppm P (TCP) + Base oil
2000 ppm P (TCP) + Base oil
4200 ppm P (TCP) + Base oil
800 ppm P (X) + Base oil
2000 ppm P (X) + Base oil
4200 ppm P (X) + Base oil
800 ppm P (ZDDP) + Base oil
2000 ppm P (ZDDP) + Base oil

Using the supplied pressure-viscosity coefficients, the fluid film thickness and therefore, lambda ratio, the lubrication regimes can be estimated for each oil over the range of speeds seen in the Stribeck test. These calculations utilised the data provided by the manufacturer to calculate the dynamic viscosity at each test temperature to give a more accurate estimate of the film thickness and therefore, the lambda ratio. Hence, it was calculated that the tests will reach the EHD at high entrainment speeds.

3.5   Wear Specimens

Specifications of the MTM and MPR test specimens are shown in Table 5, both of which, showed minimal wear throughout the Stribeck tests. It should be noted that typically, roller specimens are designed to be softer and smoother than the ring specimens to concentrate the damage onto the roller specimen

14

Table 5– Specification of test specimens.

Property	MTM Disc	MTM Ball	MPR Roller	MPR Ring
Dimensions (diameter, mm)	46 mm	¾" (19.05 mm)	12 mm cylinder	54.15 mm
Material	AISI 52100	AISI 52100	16MnCr5	16MnCr5
Surface Finish, R_a	<0.01 µm	<0.02 µm	~0.1 µm	~0.4 µm
Hardness, H_v	720-780	800-920	709 HV (58.8 HRC)	784 HV (61.9 HRC)

4 Results and Discussion

4.1 MPR results

A summary of wear track images for the MPR tests of the anti-wear additised solutions can be seen in Figure 5. Figure 6 shows results from the MPR tests; Figure 6A shows a bar chart which quantifies the amounts of micropitting as deduced from Image J analysis, Figure 6B shows the average measured friction, Figure 6C shows the average increase in wear track width of the chamfered rollers, Figure 6D shows the mean mass loss results and Figure 6E measured roughness for the counterface ring specimens. Whilst the friction was measured for all the MPR test, the measured traction coefficient on average was ~ 0.1 range and no effect of additive type or concentration was seen and hence is not shown here.

The micropitting test for base oil only showed that whilst this had the slowest onset and propagation of micropitting, it resulted in progression to more severe failure modes more quickly. This was also confirmed by the micropitting quantification Figure 6A. The base oil results in the lowest amount of micropitting and potentially showed that anti-wear additives in general give rise to an earlier onset of micropitting.

Whereas, the images for TCP show that micropitting initiates earlier at high concentrations and a higher concentration also resulted in more damage but less than what was seen for base oil. However, as shown in the Figure 6A, whilst the amount of micropitting was always more than the base oil, the amount of micropitting was not repeatable and revealed no effect of concentration or that 2000 ppm P (TCP) was the concentration that results in the most micropitting, but this would need to be studied further. In addition, the size of the micropits are consistent between concentrations.

For additive X, micropitting appears to initiate earlier and progress further at higher concentrations, however, this is backed up by results which, shows micropitting increasing as the concentration

increases. Additive X gives rise to marginally higher amounts of micropitting in comparison to TCP as shown from the images, and the micropitting quantification (Figure 6A), however, these differences are still within the overlap of error bars.

Micropitting sometimes initiates at the edge of the wear track where the chamfer begins, this is expected due to edge effects that are commonly seen with these type of micropitting experiments where there is a higher stress concentration at the edge of the wear track [48,59]. This potentially suggests that additive X is more active than TCP at protecting asperities earlier which, results in the fast formation of micropitting even at equivalent phosphorus concentrations. The size of the micropits are also comparable with TCP.

ZDDP gives rise to the early onset of micropitting and lead to extensive micropitting throughout the test across the entire wear track. The micropits appear smaller than the other ashless additives. The amounts of micropitting also increases marginally from 800 ppm P (ZDDP) to 2000 ppm P (ZDDP) showing that more ZDDP leads to a stronger effect of early asperities protection leading to more micropitting.

The friction coefficients are all in a similar range close to 0.1. However, TCP appears to have a higher friction coefficient than additive X and both of these are higher than ZDDP. It has been shown previously that ZDDP leads to an increase in friction in comparison to base oil due to maintaining asperity roughness, however, this was not seen [22,60].

There is no trend with TCP concentration and friction, which, is comparable to the micropitting quantification results. Additive X shows a slight trend with concentration as the friction increases as the concentration increases. Whereas, as the ZDDP concentration increases, the friction decreases. The base oil friction remains lower than all the other tests except ZDDP.

TCP has the lowest track width increase overall. There is also a slight decrease in as the concentration of TCP increases. Additive X has a higher wear track width increase and shows the reverse trend of increasing track width with increasing concentration. The wear track increase from ZDDP also increases with concentration and 2000 ppm P (ZDDP) has the highest track width increase despite having the lowest boundary friction as discussed in the previous section. However, in general, these are weak trends due to the large error bars. The base oil test also has the second highest track width increase. The 800 ppm P (ZDDP) could have potentially had a similar magnitude, but the significant error between repeats resulted in a reduction in the average. It was expected that the base oil test would result in a large track width increase due as the wear in this test progresses more quickly due to having no additive protection as shown from the earlier images.

These results show a very similar trend to the wear track increase results with the exception that the scale of these results are very small as the mass loss was small for all tests. The TCP tests showed a decrease in mass loss with increasing concentration, whereas additive X showed an increase in mass loss as the concentration increased. The 2000 ppm P (ZDDP) had the highest mass loss followed by the base oil test, but the 800 ppm P (ZDDP) was relatively small in comparison.
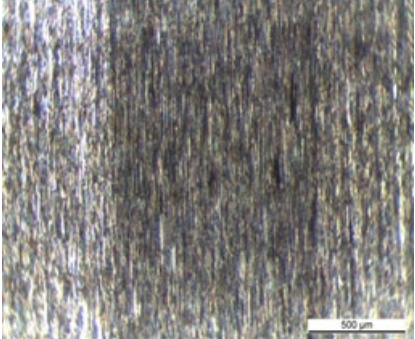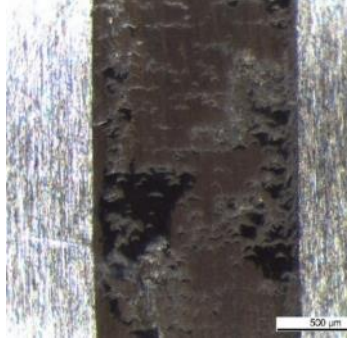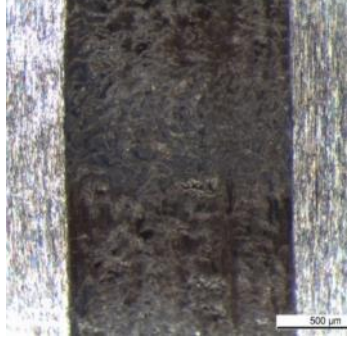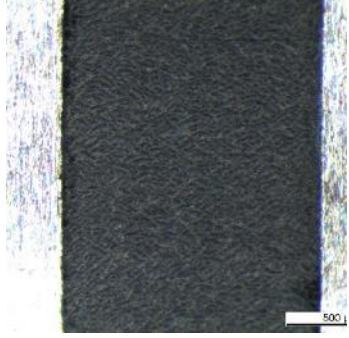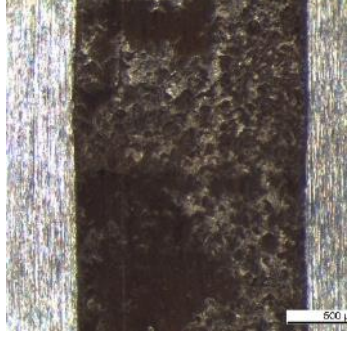
Unworn Specimen	Step 11 – 4400 k cycles
	2000 ppm P (TCP) + base oil
	2000 ppm P (X) + base oil
	2000 ppm P (ZDDP) + base oil
	Base Oil

Figure 5 – Images comparing the wear track images following the final step of the test showing the differences wear.
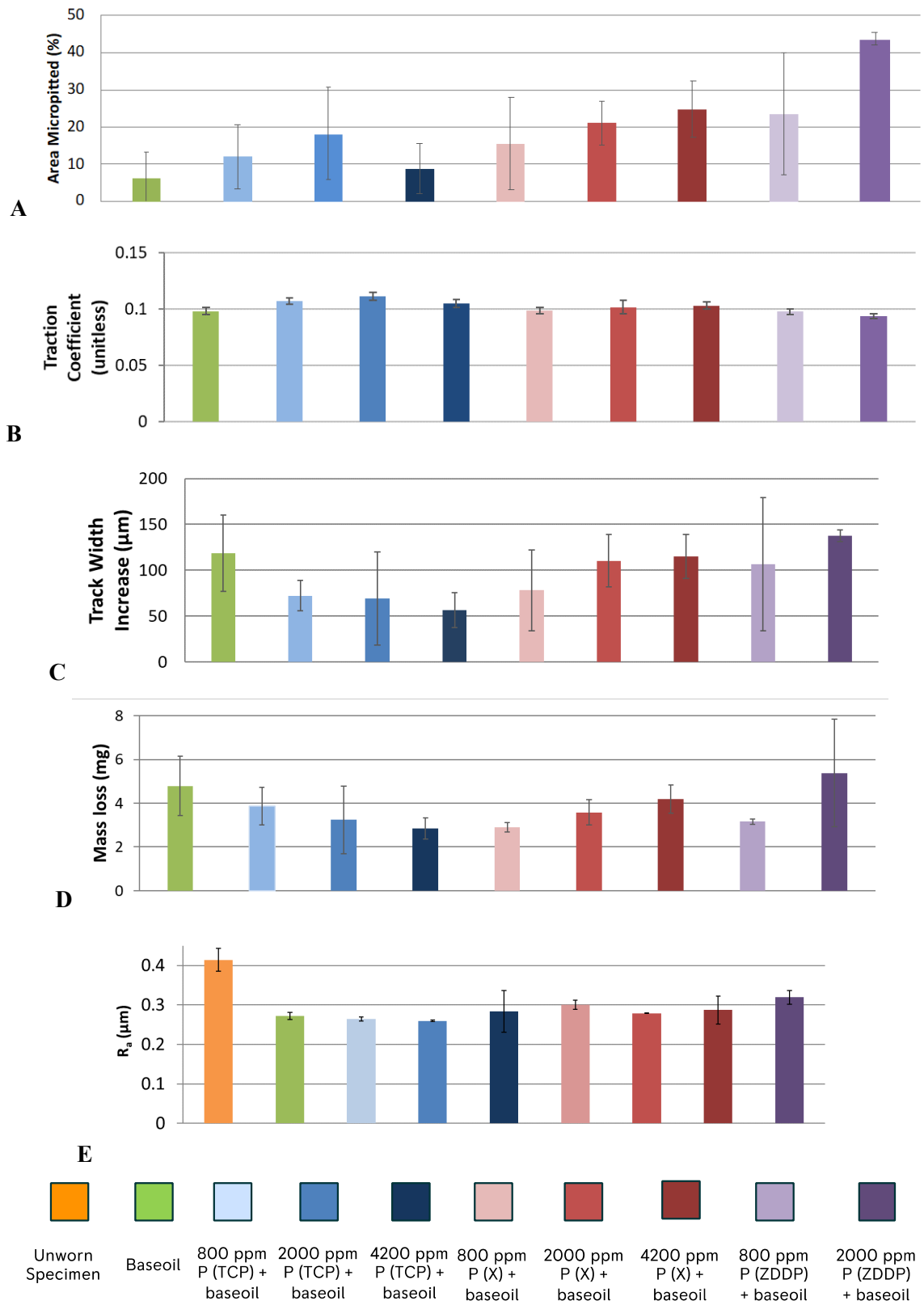
Figure 6 – MPR test results for each formulation showing there percentage area micropitted following after the 2nd step in the test regime (A), their average traction coefficient (B), their average wear track width increase (C), their mean mass loss due to wear (D) and the average change in counter face ring roughness (E).

The counterface ring roughness results in Figure 6E shows there is a substantial decrease in roughness in comparison to a fresh unworn specimen for all oils. Unfortunately, there is no roughness measurement for 800 ppm P (ZDDP). ZDDP appears to have maintained the highest roughness which, coincides with the theory that ZDDP protects and maintains asperity roughness as part of its micropitting promotion mechanism. These results for additive X are less rough and do not show any trend with concentration. The lower concentration TCP blends at 800 ppm P and 2000 ppm P have the lowest roughness followed by the base oil. These results follow a similar trend in the order ZDDP, additive X and TCP, which, show decreasing micropitting promotion (from ZDDP to TCP), reflecting how effective the additive is at maintaining asperity roughness.

The results from the FVM measurements can be seen in Figure 7; A shows a boxplot graph for the distribution of micropit depths, B shows the average centre line area roughness (S_a) of the roller specimens and then graphs C, D and E show the bearing area curve parameters; Average Core void volume, average peak material volume and average valley void volume respectively.

The pit depth results show that ZDDP has the shallowest and smallest distribution of pit depths and also shows that the pits become shallower with increasing concentration, however, this would need to be confirmed with a larger range of concentrations. Both TCP and additive X have similar depth distributions and additive X pit depth decreases with increasing concentration. However, TCP demonstrated no effect of concentration with the 4200 ppm P test having the largest pit depth distribution. The base oil test appears to have a similar pit depth distribution in comparison to the ashless additives, but it also has the most outliers which is most likely due to the wide range of different pit size for the base oil test due to it progressing to more severe macropitting failure mode.

The surface area roughness results for roller specimens show that ZDDP resulted in the lowest roughness most likely due to the small and uniform micropitting across the wear track producing a relatively smooth surface. The highest roughness was seen from TCP and then the base oil test. This was a small effect of concentration with additive X on roughness with the roughness decreasing as the concentration increased. But overall, due to the large error attained there was no distinct effect of concentration and the repeatability did not distinguish the different additives and concentrations.

From the bearing area curve parameters, the majority of the volume of the micropits in all the tests are core void volume showing that the pits are not narrow deep pits or shallow pits with large peaks (as noted from the difference in axis increments). The core and valley void volumes are on average lower for the additive containing samples in comparison to the pure baseoil. ZDDP is again the lowest by this metric showing the small size and volume of the pits in comparison to the ashless additives and the baseoil. However, TCP also at 800 and 4200 ppm P had a larger volume than the rest. But, the error bars are were large for all this data and further work is required to gain further insight to any trends.
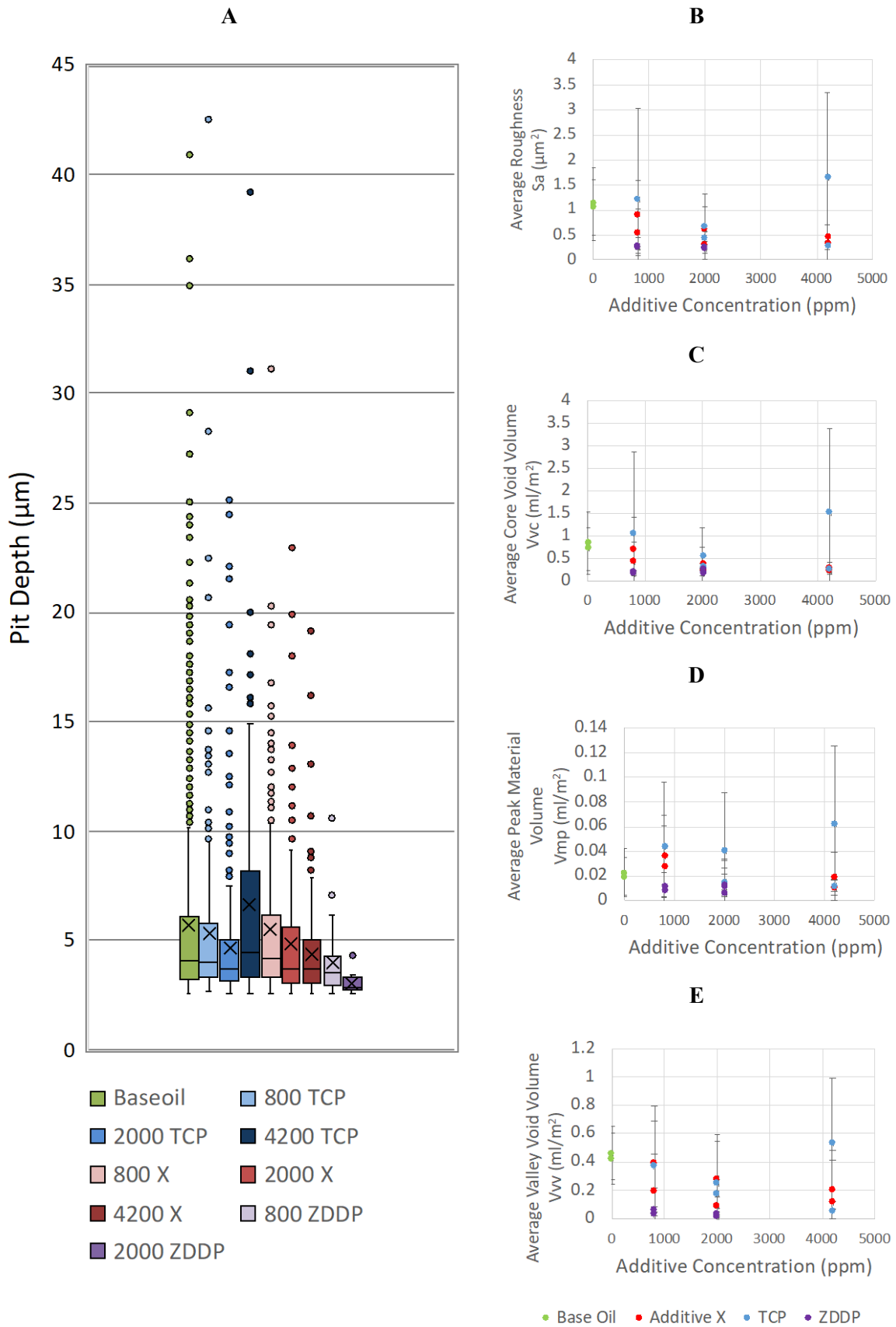
Figure 7 – FVM pit characterisation results for the different additives at varying concentrations. A shows the pit depth distribution, B shows the centre line average area roughness and C to E show the average bearing area curve parameters, core void volume, peak material volume and valley void volume.

4.2 SLIM Results

Figure 8 shows the wear track images for the ball and the disc for each additive at 2000 ppm P + base oil and the other concentrations were not included as they showed similar wear to 2000 ppm. It is immediately obvious from these results that the base oil test performs very differently to the additised blends as the ball surface shows severe wear and pitting and both the ball and disc exhibit an orange-brown discolouration at the surface.

Using the ashless anti-wear additive formulations at the same concentrations as the MPR tests (800 ppm P, 2000 ppm P and 4200 ppm P) there is very minimal wear and discolouration and no effect of concentration is seen. There is only some very faint abrasion in the wear track in the form of narrow scores and white tracks. ZDDP, however, appears different to the other additives in that there is a lot more discolouration in the wear track. It is likely the majority of this colour has come from the additive producing a visible tribofilm on the surface.

It should be noted that due to using superfinished smooth specimens, there was very minimal wear in these tests that could not be quantified using mass loss or wear track width increase (like for the MPR).

Figure 9 shows the interferometry images for base oil and the different additives at 2000 ppm P in base oil and Figure 10 shows the measured tribofilm thickness. Additional lower concentration tests were performed for TCP and additive X to determine if there was a transition to a "base oil like wear" below a minimum concentration. There are no error bars for 800 ppm P (ZDDP) as only one test was completed.

The base oil shows excessive wear, pitting and a misshapen contact on the mapper window and therefore, the film thickness was not measured as it would be interpreted as film thickness. Both ZDDP concentrations had a very thick tribofilm in comparison to the ashless additives with max film thicknesses between 120 nm to 140 nm. There is a marginal effect of concentration, with the 2000 ppm having a larger tribofilm thickness than that for 800 ppm. Despite the error bars being large, the difference is outside of the error bar range. There is a plateau of film thickness which, may back up the theory of Zhang et al. [38] on the plastic deformation of the tribofilm leading to an increase in contact area which, consequently decreases the shear stress enough to prevent tribofilm formation. However, even though subsequent images from this plateau region of Figure 10 have subtle differences in features in the interferometry images, it is unclear whether these are due to new tribofilm formation or tribofilm removal. The thickness of these films could be responsible for the difference in wear track appearance in Figure 8; ZDDP appears to affect the surface more than the ashless additives, but still provides wear protection. But this test does not produce large amounts of wear, so the wear performance cannot be justified as much as from the MPR.

The interferometry images for the ashless additives show thin tribofilm films ~30 nm are produced and the fact that these do not progress onto the base oil like wear shows they are providing adequate protection despite being thin. The marginally darker colour for additive X may suggest it forms a slightly thicker tribofilm film that TCP however, the measured tribofilms are both in the 30 nm range. However, the measurement may incur some error due to the limitation of the SLIM detecting tribofilms below 30 nm and due to the SLIM being calibrated to ZDDP tribofilms, but it is assumed that the optical characteristics of ashless phosphorus based tribofilms are similar to phosphorus tribofilms derived from ZDDP as previously discussed by Benedet [23]. The film thickness for the 100 ppm P TCP test was not measured due to it producing a worn surface resembling the wear from the test for base oil, therefore it could not protect the surface at that low concentration. But when additive X was tested at 100 ppm P, it provided sufficient protection to prevent the base oil like wear from occurring showing additive X is more effective that TCP at lower concentrations.

From observing the progression of the interferometry images, it appears the subtle changes in the images in subsequent steps are as a result of removal and reformation of tribofilm. This opposes the theory suggested for ZDDP where plastic deformation of the tribofilm results in a larger contact area decreasing the shear stress below that required for tribofilm formation [38,43,61]. However, it could be that thinner ashless additives are weaker and therefore, more susceptible to being sheared off.

Whilst Stribeck curves were generated for the all the tests at the start and end of the test regime, due to showing similar trends, only the curves for the additives at 2000 ppm and base oil are shown in Figure 11. In general, the Stribeck curves demonstrated an increase in friction across all lubrication regimes between the start and end of the test. This was expected due to the wear test producing rougher surface therefore influencing the measured friction. There was no effect of concentration on the Stribeck curves for the same additive. However, the effect each additive has on friction across the lubrication regimes can be seen in Figure 11 and this effect was also found to be more prominent at the higher additive concentration of 2000 ppm P. From the initial Stribeck curves, ZDDP has higher friction across all regimes, however, the size of the error bars show how much variability there was in the results for ZDDP. This could be an effect of how quickly ZDDP interacts with the surface therefore influencing friction more quickly that the other additives. The other additive and base oil have similar a friction on the initial Stribeck curves. However from the final Stribeck curves, a different trend is seen where ZDDP has the lowest friction in the boundary regime. This is similar to what was found in the MPR friction results (Figure 6). The other additives formulations and the base oil have a similar friction coefficient at final striction curve are all within their corresponding error bars overlap.

The traction coefficients that are measured throughout the entire test can in Figure 12 and these show a "spike" after certain periods of time showing when the Stribeck curves were measured. Despite 7 Stribeck curves being recorded for each test, only the start and end Stribeck curves were shown in

Figure 11 as their interpretation provided no additional insight. In comparison to the Stribeck curves, the Figure 12 shows the boundary friction measured throughout the test. Again there was minimal effect of concentration between the same additive, but there was a difference between the different additives which was more pronounced at the higher concentration of 2000 ppm P. The base oil has the highest boundary friction towards the end of the test most likely due to the excessive wear produced in this test. ZDDP initial has the higher friction and then decreases and stabilizes. This could be attributed to the rapid formation of the ZDDP tribofilm compared to the ashless additives. TCP has the lowest boundary friction towards the end of the test. This could be due to TCP being the slowest at forming a detectable tribofilm. But as shown from the wear track images, this additive results in minimal wear forming showing the additive provides sufficient protection against wear.

	Ball	Disc
Base oil		
2000 ppm P (TCP) + Base oil		
2000 ppm P (X) + Base oil		
2000 ppm P (ZDDP) + Base oil		
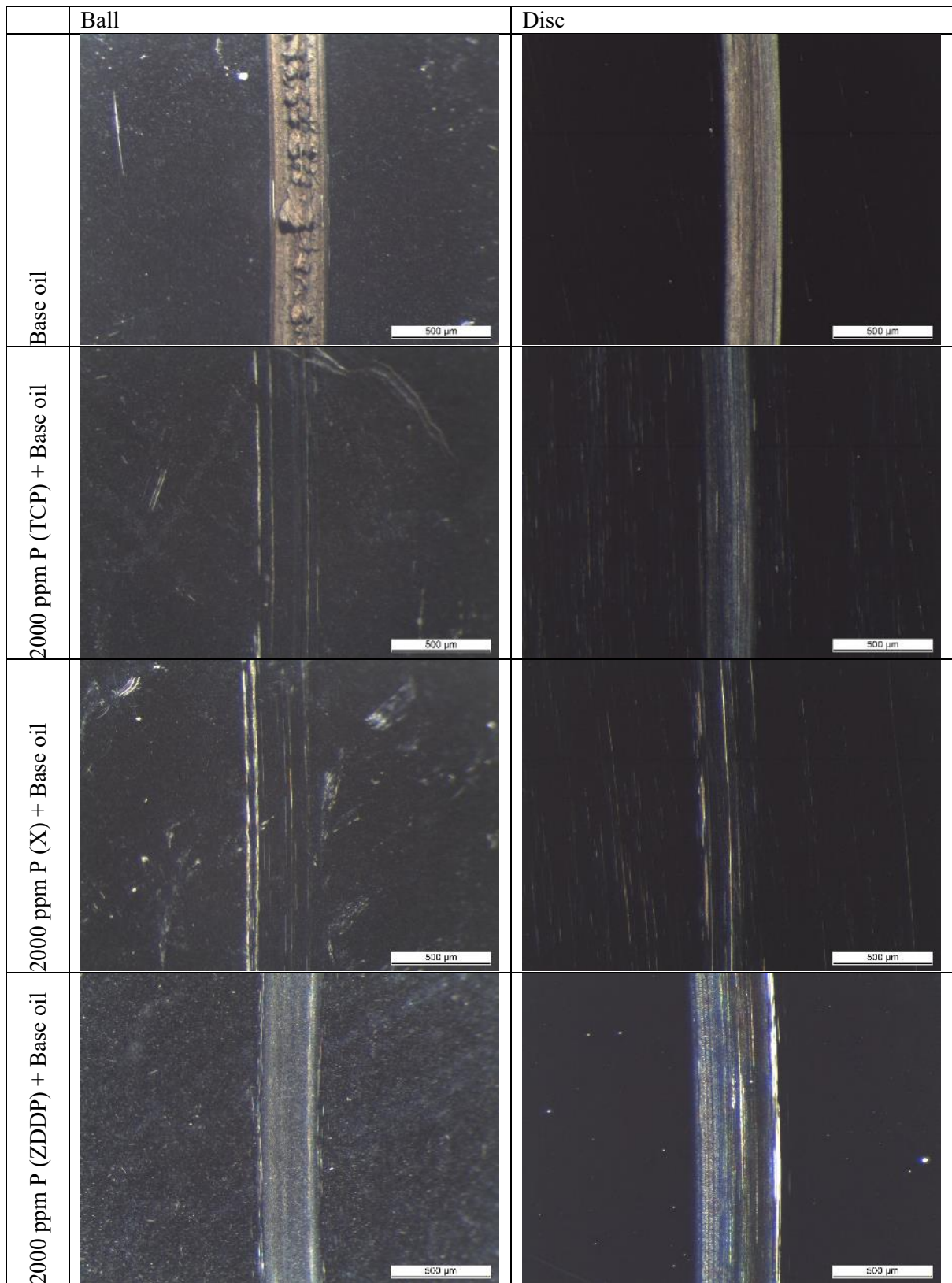
Figure 8 – Wear track optical microscope images of ball and disc specimens from the MTM-SLIM tests

25
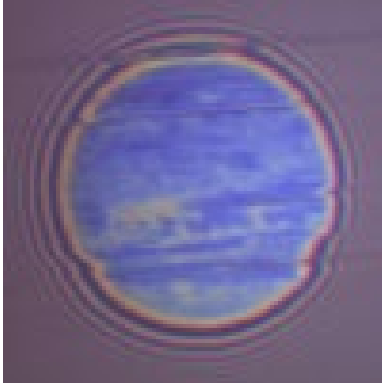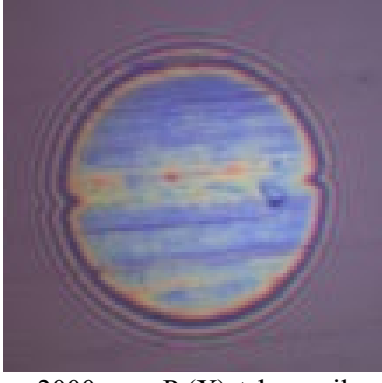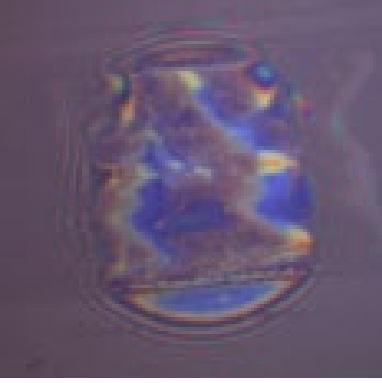
Beginning of the Test	Interferometry image from the end of test
	2000 ppm P (TCP) + base oil
	2000 ppm P (X) + base oil
	2000 ppm P (ZDDP) + base oil
	Base Oil

Figure 9 – Images comparing the interferometry images following the final step of the test showing the differences in film thickness and wear.
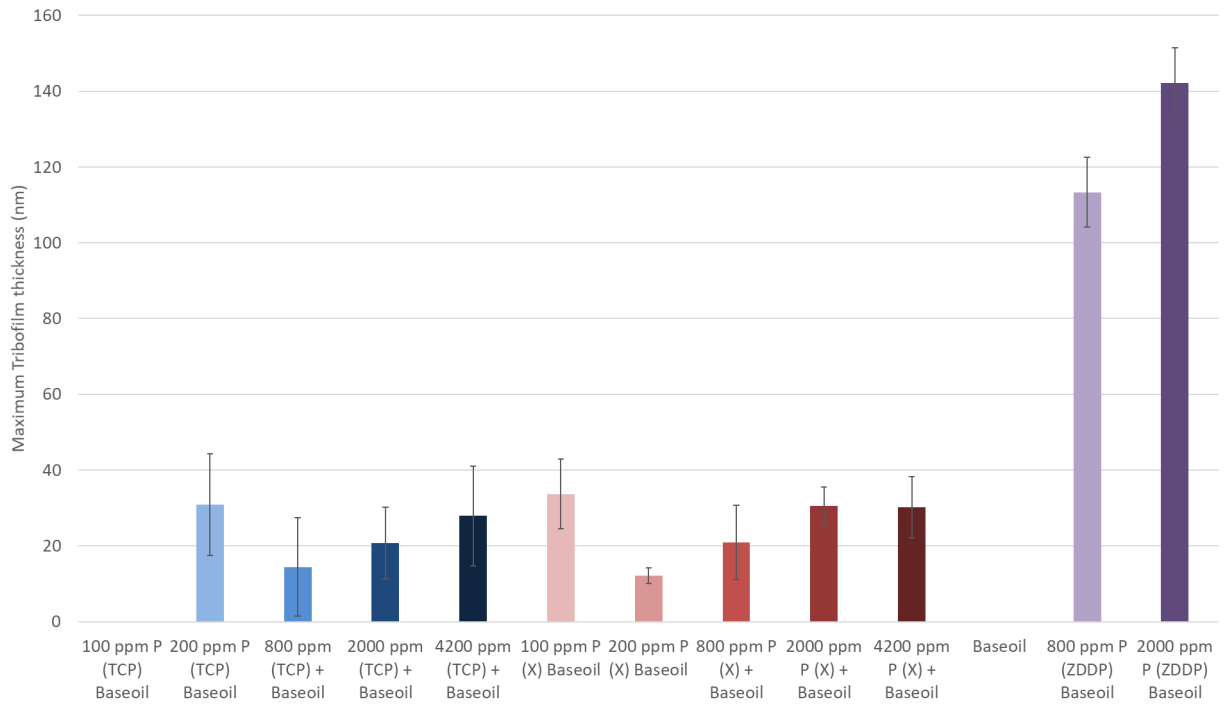
Figure 10 – The maximum measured tribofilm thickness for all of the formulations tested (no tribofilm was measured for 100 ppm P (TCP) and base oil due to showing excessive wear.
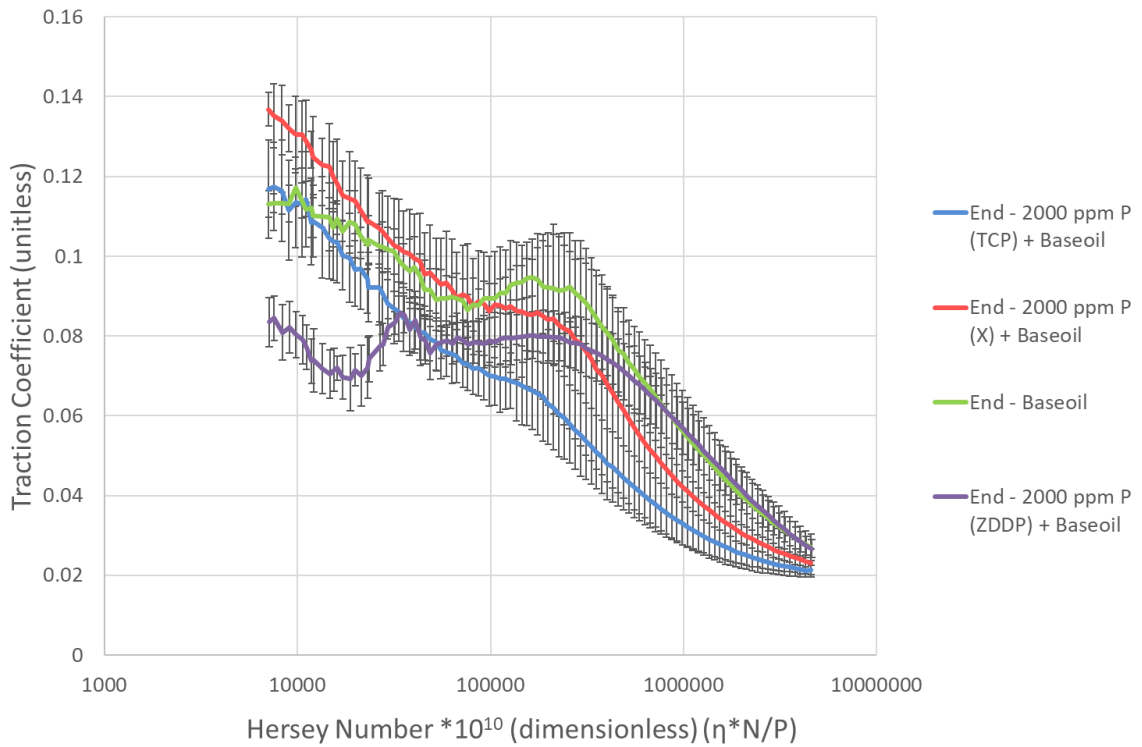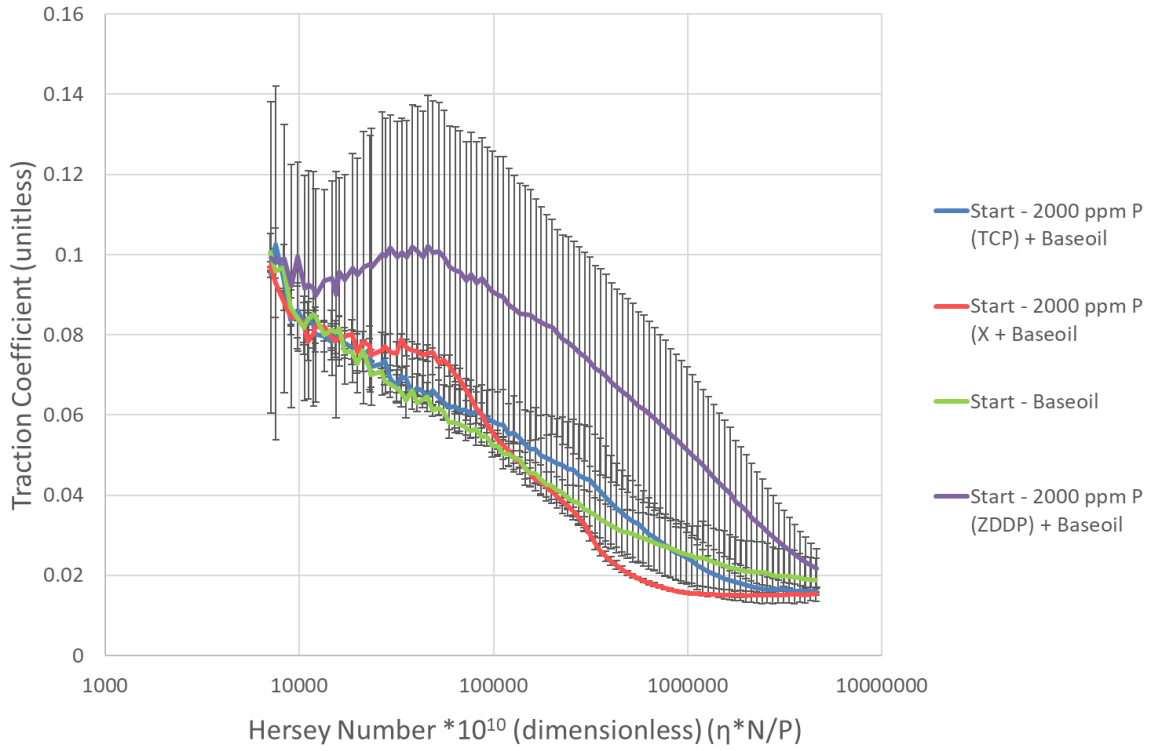
Figure 11 – Comparison between the different anti-wear additives at 2000 ppm P at the start and end of the test
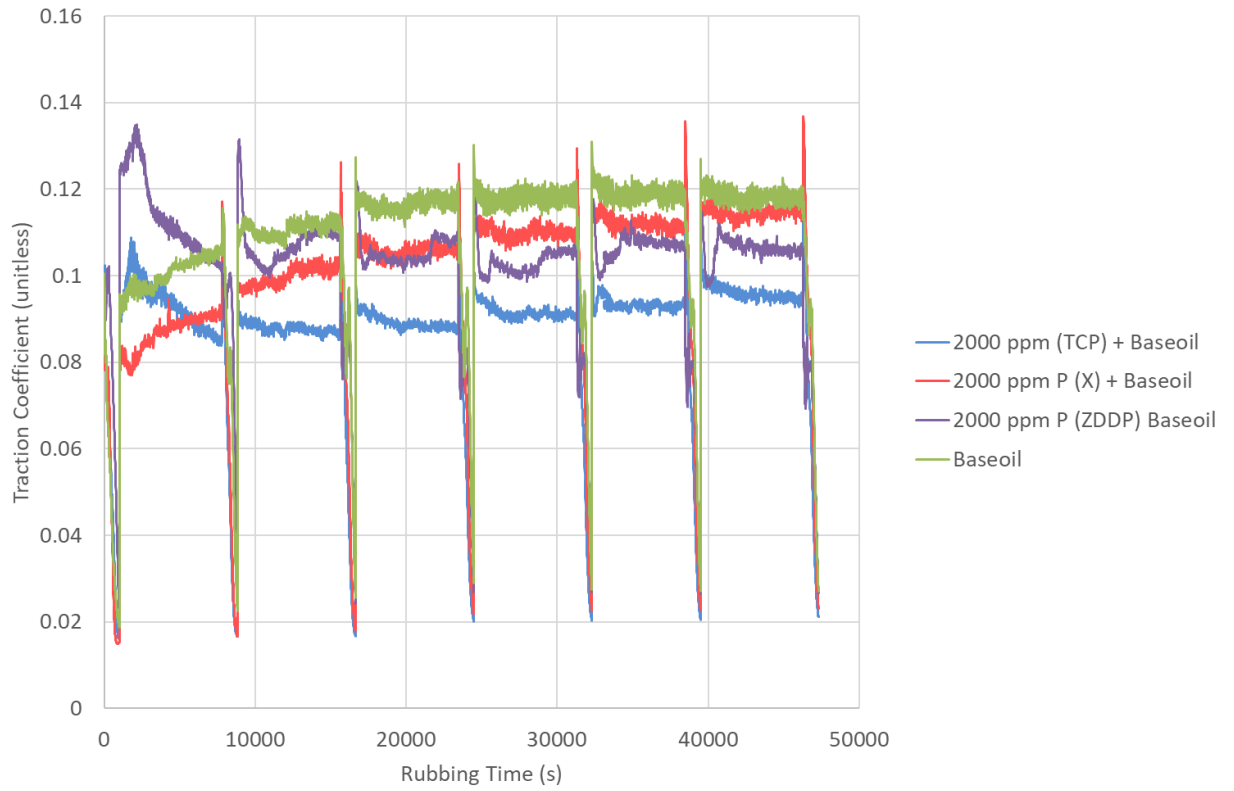
Figure 12 – The overall friction throughout the test for all the different anti-wear additives at 2000 ppm P.

5   Conclusions

Overall it has been shown that a variety of methods have been used to evaluate three different anti-wear additives at different concentrations to understand whether ashless additives also promote micropitting like it has been shown for ZDDP.

The MPR results found that TCP showed a slower progression and a smaller amount of micropitting compared to the other additives, there did not appear to be an effect of concentration and the micropits were larger than those produced for ZDDP. Additive X showed a faster progression of micropitting and more micropitting than TCP, but less than ZDDP which, appears to increase slightly with increasing concentration. The micropits were a similar size to TCP, but larger than those produced from ZDDP. ZDDP showed the fastest progression and larger amount of micropitting, which, appeared to increase with concentration. The micropits were smaller than those produced for the other additives. Base oil had the slowest progression of micropitting, but quickly propagated into more severe failures like macropitting and produced no colours on the surface. The FVM results also reinforce that ZDDP formed smaller micropits which also had a smaller size distribution than the ashless additives.

The track width results demonstrated that TCP had the lowest increase in track width increase and showed no effect of concentration. Additive X has some effect of concentration showing an increasing track width increase with high additive X concentrations. The base oil had the second highest track width increase. However, ZDDP had the highest track width increase, which, increased with higher concentrations. This highlighted that despite not progressing to more severe failure modes like base oil, a substantial amount of wear was seen from extensive micropitting alone showing the dangers of micropitting. The same trend was also reflected in the mass loss results.

From the roughness results, it was found the base oil test had the lowest average ring roughness and was similar to TCP. Additive X had a slightly higher roughness, but ZDDP had the highest. This agrees with theory of ZDDP protecting asperities early, which prevents running in by protecting asperities and therefore, roughness, which, promotes micropitting.

The MTM-SLIM results demonstrated from the wear track images that the base oil shows severe wear and pitting. The ashless additives show minimal wear with only some abrasion showing protection of the surface. As the concentration is decreased, 100 ppm P (TCP) has wear just like base oil, but additive X only shows some initiation of that kind of wear, suggesting that additive X is more effective at protecting the surface at lower concentrations. ZDDP visually affects the surface more than the others as shown from more discolouration of the wear track, but no pitting was seen.

From the interferometry images found that the base oil produces a very misshapen and dark contact clearly indicating wear as confirmed by the optical images and that the tribofilm thickness should not

be measured. TCP forms a very thin tribofilm of maximum thickness ~30 nm, which, also forms slowly, but it still sufficient for the wear not to progress into the failure mode seen with base oil except for 100 ppm. Additive X arguably forms a slightly thicker tribofilm as seen from the images, however, the measurements show the thickness is similar to TCP. ZDDP forms a very thick tribofilm ~80-140 nm very quickly in comparison.

The rapid action of the ZDDP additive was highlighted by an increase in friction on the initial Stribeck curves but then decreases resulting in the lowest friction across all the other additives. The ashless additive showed similar friction performance but the base oil test gave the highest frication towards the end of the test most likely due to having more severe wear.

Overall, it can be seen that TCP and additive X promote micropitting to a much lesser extent than ZDDP. This could be attributed to their slower and thinner tribofilm formation that allows surfaces to "run-in" and, therefore, do not maintain high asperity contact pressures as aggressively as ZDDP. This delays the onset of micropitting initiation however, micropitting does seem to initiate earlier than for the base oil tests as the protection is sufficient to protect against more severe failure modes. The study has clearly shown the catastrophic effects of a less severe wear mechanism like micropitting as ZDDP promoted micropitting to such an extent that the amount of wear has surpassed the base oil with no additive protection.

6 Acknowledgements

7 Declaration of Conflicting Interests

8 Funding

9 References

1. Mortier RM, Fox MF, Orszulik S. *Chemistry and Technology of Lubricants*. Dordrecht: Springer Netherlands, 2011.

2. Shell Aviation Limited. The AeroShell Book. *Aviation* 2003; 196.

3. Airey J, Spencer M, Greenwood R, et al. The Effect of Gas Turbine Lubricant Base Oil Molecular Structure on Friction. *Tribol Int* 2020; 146: 11.

4. Stachowiak G, Batchelor AW. Chapter 8: Boundary and Extreme Pressure Lubrication. In: *Engineering Tribology*. 2011, pp. 425–484.

5. Lainé E, Olver A V., Beveridge TA. Effect of lubricants on micropitting and wear. *Tribol Int*. Epub ahead of print 2008. DOI: 10.1016/j.triboint.2008.03.016.

6. Balcombe R, Fowell MT, Olver A V., et al. A coupled approach for rolling contact fatigue cracks in the hydrodynamic lubrication regime: The importance of fluid/solid interactions. *Wear* 2011; 271: 720–733.

7. Balcombe R. *A study of rolling contact fatigue cracks in lubricated contacts*. Imperial College London, 2012.

8. Webster MN, Norbart CJ. An experimental investigation of micropitting using a roller disc machine. *Tribol Trans* 1995; 38: 883–93.

9. Olver AV. Micropitting of gear teeth: design solutions. In: *Aerotech'95, Birmingham*. Birmingham: London: Institute of Mechanical Engineerin, 1995.

10. Spikes HA, Olver A V, Macpherson PB. *Wear in Rolling Contacts*. 1986.

11. Way S. Pitting due to rolling contact. *J Appl Mech* 1935; 57: 49–58.

12. Berthe D, Flamand L, Foucher D, et al. Micropitting in Hertzian contacts. *ASME J Lubr Technol Trans* 1980; 102: 478–89.

13. Zhou RS, Cheng HS, Mura T. Micropitting in rolling and sliding contact under mixed lubrication. *J Tribol* 1989; 111: 605–13.

14. Cardis AB, Webster MN. Gear oil micropitting evaluation. *Gear Technol* 2000; 17: 30–35.

15. Graham RC. *Pitting of hard steel rolling-sliding elastohydrodynamically lubricated line contacts*. Imperical College London, 1979.

16. Brechot P, Cardis AB, Murphy WR, et al. Micropitting resistant industrial gear oils with balanced performance. *Ind Lubr Tribol* 2000; 52: 125–136.

17. Nakajima A. Effect of asperity interacting frequency on surface durability. In: *International symposium on gearing and power transmissions*. Tokyo, 1981, p. 26.

18. Nakajima A, Ichimaru K, Hirano F. Effects of combination of rolling direction and sliding direction on pitting of roller. *J Synth Lubr Eng* 1983; 4: 93–8.

19. Winter H, Oster P. Influence of lubrication on pitting and micropitting resistance of gears. *Gear Technol* 1990; 7: 16–23.

20. Hohn BR, Oste P, Emmert S. Micropitting in case-carburised gears - FZG micropitting test. *VDI Ber* 1996; 1230: 331–44.

21. Bull SJ, Evans JT, Shaw BA, et al. The effect of the white layer on micropitting and surface contact fatigue failure of nitrided gears. *Proc Inst Mech Eng Part J J Eng Tribol* 1999; 213: 305–13.

22. Ueda M, Spikes H, Kadiric A. In-situ observations of the effect of the ZDDP tribofilm growth on micropitting. *Tribol Int* 2019; 138: 342–352.

23. Benedet JFL. *Low and Zero SAPS Antiwear Additives for Engine Oils*. Imperial College of Science, Technology and Medicine, London, 2012.

24. Topolovec-Miklozic K, Forbus TR, Spikes HA. Film thickness and roughness of ZDDP antiwear films. *Tribol Lett* 2007; 26: 161–171.

25. Johnson D, Bachus M, Hils J. Interaction between Lubricants Containing Phosphate Ester Additives and Stainless Steels. *Lubricants* 2013; 1: 48–60.

26. Sheasby JS, Caughlin T a., Mackwood W a. The effect of steel hardness on the performance of antiwear additives. *Wear* 1996; 201: 209–216.

27. Gauthier A, Montes H, Georges J. Boundary Lubrication with Tricresylphosphate (TCP). Importance of Corrosive Wear. *ASLE Trans* 1982; 445–455.

28. Perez JM, Ku CS, Pei P, et al. Characterization of Tricresylphosphate Lubricating Films by Micro- Fourier Transform Infrared Spectroscopy. *Tribol Trans* 1990; 131–139.

29. Trivedi HK, Forster NH, Rosado L. Rolling contact fatigue evaluation of advanced bearing steels with and without the oil anti-wear additive tricresyl phosphate. *Tribol Lett* 2011; 41: 597–605.

30. Soltanahmadi S, Morina A, van Eijk MCP, et al. Tribochemical study of micropitting in tribocorrosive lubricated contacts: The influence of water and relative humidity. *Tribol Int*. Epub ahead of print 2017. DOI: 10.1016/j.triboint.2016.11.031.

31. Trivedi HK, Forster NH, Rosado L. Rolling contact fatigue evaluation of advanced bearing steels with and without the oil anti-wear additive tricresyl phosphate. *Tribol Lett*. Epub ahead of print 2011. DOI: 10.1007/s11249-010-9738-6.

32. Topolovec-Miklozic K, Forbus TR, Spikes HA. Film thickness and roughness of ZDDP antiwear films. *Tribol Lett*. Epub ahead of print 2007. DOI: 10.1007/s11249-006-9189-2.

33. Soltanahmadi S, Morina A, Van Eijk MCP, et al. Investigation of the effect of a diamine-based friction modifier on micropitting and the properties of tribofilms in rolling-sliding contacts. *J Phys D Appl Phys*. Epub ahead of print 2016. DOI: 10.1088/0022-3727/49/50/505302.

34. Fujita H, Spikes HA. Study of zinc dialkyldithiophosphate antiwear film formation and removal processes, part II: Kinetic model. *Tribol Trans* 2005; 48: 567–575.

35. Hsu SM, Gates RS. Boundary lubricating films: Formation and lubrication mechanism. *Tribol*

Int 2005; 38: 305–312.

36.   FUJITA H, SPIKES HA. Study of Zinc Dialkyldithiophosphate Antiwear Film Formation and Removal Processes, Part II: Kinetic Model. *Tribol Trans* 2005; 48: 567–575.

37.   Gosvami NN, Bares JA, Mangolini F, et al. Mechanisms of antiwear tribofilm growth revealed in situ by single-asperity sliding contacts. *Science (80-)* 2015; 348: 102–106.

38.   Zhang J, Spikes H. On the Mechanism of ZDDP Antiwear Film Formation. *Tribol Lett* 2016; 63: 24.

39.   Spikes H. The history and mechanisms of ZDDP. *Tribol Lett* 2004; 17: 469–489.

40.   Morina A, Neville A. Tribofilms: Aspects of formation, stability and removal. *J Phys D Appl Phys*. Epub ahead of print 2007. DOI: 10.1088/0022-3727/40/18/S08.

41.   Guan B, Pochopien BA, Wright DS. The chemistry, mechanism and function of tricresyl phosphate (TCP) as an anti-wear lubricant additive. *Lubr Sci* 2015; 123–134.

42.   Zhang J, Spikes H. On the Mechanism of ZDDP Antiwear Film Formation. *Tribol Lett*. Epub ahead of print 2016. DOI: 10.1007/s11249-016-0706-7.

43.   Spikes H. Stress-augmented thermal activation: Tribology feels the force. *Friction* 2018; 6: 1–31.

44.   Dawczyk J, Ware E, Ardakani M, et al. Use of FIB to Study ZDDP Tribofilms. *Tribol Lett* 2018; 66: 1–8.

45.   Fujita H, Glovnea RP, Spikes HA. Study of zinc dialkydithiophosphate antiwear film formation and removal processes, part I: Experimental. *Tribol Trans* 2005; 48: 558–566.

46.   Jones RB, Coy RC. The chemistry of the thermal degradation of zinc dialkyldithiophosphate additives. *ASLE Trans* 1981; 24: 91–97.

47.   Lainé E, Olver A V., Lekstrom MF, et al. The effect of a friction modifier additive on micropitting. *Tribol Trans*. Epub ahead of print 2009. DOI: 10.1080/10402000902745507.

48.   Benyajati C, Olver A V, Hamer J. An experimental study of micropitting, using a new miniature test-rig. *Transient Process Tribol* 2004; 601–611.

49.   Benyajati C, Olver A V, Hamer J. *An experimental study of micropitting, using a new miniature test-rig*.

50.   Olver AV, Dini D, Lainé E, et al. Roughness and Lubricant Chemistry Effects in Micropitting. In: *AGMA Fall Technical Meeting*. Detroit, MI: American Gear Manufacturers Association, 2007.

51.   Sayles RS, Macpherson PB. Influence of wear debris on rolling contact fatigue. *Roll Contact Fatigue Test Bear Steels Symp, (Phoenix, US.a May 12-14, 1981), JJC Hoo (Astm Publ* 1982; ASTM STP 7: 255–274.

52.   Nikas GK, Sayles RS, Ioannides E. Effects of debris particles in sliding/rolling elastohydrodynamic contacts. *Proc Inst Mech Eng Part J J Eng Tribol* 1998; 212: 333–342.

53.   Olver A V. Testing Transmission Lubricants: The Importance of Thermal Response. *Proc Inst Mech Eng Part G J Aerosp Eng*. Epub ahead of print 1991. DOI: 10.1243/PIME_PROC_1991_205_235_02.

54.   Sanchez-Rubio M, Chinas-Castillo F, Ruiz-Aquino F, et al. A new focus on the Walther equation for lubricant viscosity determination. *Lubr Sci* 2006; 18: 95–107.

55.   Moore AJ. The behaviour of lubricants in elastohydrodynamic contacts. *Proc Inst Mech Eng Part J J Eng Tribol* 1997; 211: 91–106.

56.   Spikes HA, Cann PM. The development and application of the spacer layer imaging method for measuring lubricant film thickness H A Spikes and. *Proc Inst Mech Eng* 2001; 2015: 261–278.

57.   Cann PM, Spikes HA, Hutchinson J. The Development of a Spacer Layer Imaging Method (SLIM) for Mapping Elastohydrodynamic Contacts. *Tribol Trans* 1996; 39: 915–921.

58.   Newton L, Senin N, Gomez C, et al. Areal topography measurement of metal additive surfaces using focus variation microscopy. *Addit Manuf* 2019; 25: 365–389.

59.   Rycerz P. *Propagation of surface initiated rolling contact fatigue cracks in bearing steel*. 2014.

60.   Soltanahmadi S. *Tribochemical investigation of micropitting in rolling-element bearing applications: the influence of lubricant additives and water contamination*. 2017.

61.   Ueda M, Spikes H, Kadiric A. In-situ observations of the effect of the ZDDP tribofilm growth on micropitting. *Tribol Int* 2019; 138: 342–352.

62.   Jaeger JC. Moving sources of heat and the temperature of sliding contacts. *Proc R Soe New South Wales* 1942; 56: 203.

63. Rycerz P. *Propagation of surface initiated rolling contact fatigue cracks in bearing steel*. Imperial College London, 2014. Epub ahead of print 2014. DOI: 10.1016/j.ijfatigue.2016.12.004.

64. Rycerz P, Kadiric A. The Influence of Slide–Roll Ratio on the Extent of Micropitting Damage in Rolling–Sliding Contacts Pertinent to Gear Applications. *Tribol Lett* 2019; 67: 1–20.

65. ASTM International. ASTM D341-09: Standard Practice for Viscosity-Temperature Charts for Liquid Petroleum. *ASTM Int West Conshohocken, PA*. Epub ahead of print 2009. DOI: 10.1520/D0341-09.2.

66. ASTM International. Standard Test Method for Kinematic Viscosity of Transparent and Opaque Liquids (and Calculation of Dynamic Viscosity) 1. *Annu B ASTM Stand* 2010; i: 1–10.

10 Appendix

10.1 Calculation for temperature rise at the MPR contact inlet

Due to the conditions within the contact, the actual temperature of the lubricant in the inlet will increase in comparison to the bulk. Therefore, this temperature rise can be calculated which, allows a more accurate calculation of the viscosity of the fluid in the contact and therefore, the film thickness. This can be estimated using Jaegers theory of moving hot spots as reviewing by Olver [53,62]. The equations are based on a model that assumes that frictional heat is created in the contact between both specimens and is then conducted away into the surfaces of the specimens [63]. Jaegers theory of moving hot spots proposed three different equations for the temperature rise in the contact depending on the geometry of the contact. The was one for infinite roller where $l \to \infty$, one for a thin disc where the disc radius is more than the width and one for small discs with a thick shaft where the width of the disc is less than the disc radius which, is less than the shaft length. It is recognised that the complex geometry of the MPR contact does not fit perfectly into one of these categories due to the roller and disc falling into different categories, the thin disc equation was used a good assumption of temperature rise in the contact [59,64].

$$Thin\ Discs,\ M_R = \left\{ 8.88(hk)^{\frac{1}{2}} l^{\frac{1}{2}} R \frac{I_1(nR)}{I_0(nR)} \right\}^{-1}$$

$$where\ n = \left(\frac{2h}{kl}\right)^{-1}$$

$$B_i = \frac{1}{2bl} \frac{1}{k_i} \left(\frac{\chi_i b}{u_i}\right)^{\frac{1}{2}}\ where\ i = 1,\ 2\ (Roller\ or\ ring)$$

$$\alpha = \frac{1.06 B_2 + M_2}{1.06(B_1 + B_2) + M_1 + M_2}$$

$$Inlet\ Temperature\ (Contact\ Temp),\ (T_C)_1 = (W\mu\Delta u) \times \alpha \times (1.60 B_1 + M_1) + T_A$$

ρ is the steel density, b is the contact half width, l is axial length of contact, k is the steel thermal conductivity, Cp is the specific heat capacity of steel, X is the thermal diffusivity, u_1 and u_2 are the surface speeds of the roller and ring respectively, Δu (u_1-u_2) is the sliding speed, μ is the coefficient of friction, T_A is the ambient temperature, W is the total load, h is the convective heat transfer coefficient and I_1 and I_0 are Bessel Functions.

The equations below show how the convective heat transfer coefficient was calculated based on the equations for forced convection heat transfer past plane surfaces for laminar flow [53] and also the thermal diffusivity.

$$Reynold\ number,\ (N_{RE})_L = \frac{UL}{\upsilon}$$

$$Prandtl\ Number, N_{PR} = \frac{\eta C_p}{k}$$

$$Nusselt\ Number,\ (N_{NU})_L = 0.664(N_{RE})_L^{\frac{1}{2}}(N_{PR})^{\frac{1}{3}}$$

$$Nusselt\ Number,\ (N_{NU})_L = \frac{hL}{k}$$

$$Convective\ Heat\ Transfer\ Coefficient,\ h = \frac{(N_{NU})_L k}{L}$$

$$Thermal\ Diffusivity, X = \frac{k}{\rho C_p}$$

ρ is the oil density, U is the fluid free stream velocity, L is the plate length, υ is the kinematic viscosity, η is the dynamic viscosity, k is the oil thermal conductivity at 100°C and C_p is the specific heat capacity at 100°C. Once the temperature rise had been calculated, the Walther equation could be used to calculate the kinematic viscosity at that temperature [54]. The Walther equation is also the basis of method ASTM D341 which, was used to calculate the kinematic viscosities of the oils used in **Error! Reference source not found.** and this calculation is shown in 10.3.

10.2 Kinematic Viscosities of the base oils

Table 10-1 shows the measured kinematic viscosities of the base oils used for investigating chain length and the number of ester groups and Table 10-2 shows the variation in molecular weight between these base oils.

Table 10-1 – Table listing some of the measured properties of the base oils investigating chain length and the number of esters in a polyol ester (**Error! Reference source not found.**).

Ester description	Kinematic Viscosity at 40 °C (cSt)	Kinematic Viscosity at 100 °C (cSt)
MONOPE with all n-C5 acid	15.4	3.6
MONOPE with all *n*-C7 acid	21.3	4.6

Ester description		
MONOPE with all *n*-C9 acid	30.3	5.9
TMP with all *n*-C7 acid	14.0	3.4
NGP with all *n*-C7 acid	5.6	1.9

Table 10-2 – Table displaying the number of each element in the compound and hence, the molecular weights of the base oils.

Ester description	Carbon	Hydrogen	Oxygen	Molecular Weight g/mol
MONOPE with all n-C5 acid	41	76	8	472.619
MONOPE with all *n*-C7 acid	33	60	8	584.835
MONOPE with all *n*-C9 acid	25	44	8	697.051
TMP with all *n*-C7 acid	27	50	6	470.691
NGP with all *n*-C7 acid	19	36	4	328.493

Table 10-3 shows the measured kinematic viscosities of the base oils used for investigating the effect of molecular branching.

Table 10-3 - Table listing some of the measured properties of the base oils investigating the degree of molecular branching in a polyol ester (**Error! Reference source not found.**).

Ester description	Kinematic Viscosity at 40 °C (cSt)	Kinematic Viscosity at 100 °C (cSt)
MONOPE with all NC8	25.52	5.24
MONOPE with NC8: EH of 75:25	27.53	5.33
MONOPE with NC8: EH of 50:50	30.99	5.5
MONOPE with NC8: EH of 25:75	35.48	5.74
MONOPE with all NC8	44.12	6.24

The kinematic viscosities for the formulated oils provided are shown in Table 10-4 with their corresponding viscosities at 40 and 100 °C.

Table 10-4- Table of the fully formulated blends viscosities at 40 and 100°C.

	Kinematic Viscosity at 40 °C (cSt)/ (mm^2/ s)	Kinematic Viscosity at 100 °C (cSt))/ (mm^2/ s)
High	66.1	8.04
Medium High	52.4	6.93
Medium Low	31.5	4.99
Low	12.6	3.08

10.3 Temperature and viscosity prediction using ASTM D341

The ASTM method D341 was used to calculate the temperature at which, each oil has certain viscosity [65]. The example shown here is for the MONOPE C9 base oil, but the same method was done for the other base oils too. To predict the temperatures and kinematic viscosities, at least two measured viscosities are needed for each oil at known temperatures. Using equations (10-1), (10-2) and (10-3), the kinematic viscosities can be calculated by plotting a line of LogT against LogLogZ as shown in Figure 10-1.

$$LogLogZ = A - BLogT \qquad \text{(10-1)}$$

$$Z = v + e^{\left(-1.47-1.84v-0.51v^2\right)} \qquad \text{(10-2)}$$

$$v = (Z - 0.7) + e^{\left(0.7487-3.295(Z-0.7)+0.6119(Z-0.7)^2-0.3193(Z-0.7)^3\right)} \qquad \text{(10-3)}$$

(10-4)

Temperature (°C)	LogT (T converted into K)	Kinematic Viscosity (cSt)	LogLogZ
40	2.4958	30.5	0.1744
100	2.5719	5.99	-0.0833
108.9	2.5821	5.407	-0.1047

Table 10-5 - Table showing the measured kinematic viscosities and at measured temperatures and the calculated values for LogT and LogLogZ.

The kinematic viscosities at 40 and 100°C were provided by the supplier and the viscosity at 108.9°C was measured using ASTM D445 to confirm the oil had a viscosity of 5 cSt and also to gather another data point to feed back into the viscosity prediction to improve its accuracy [66].
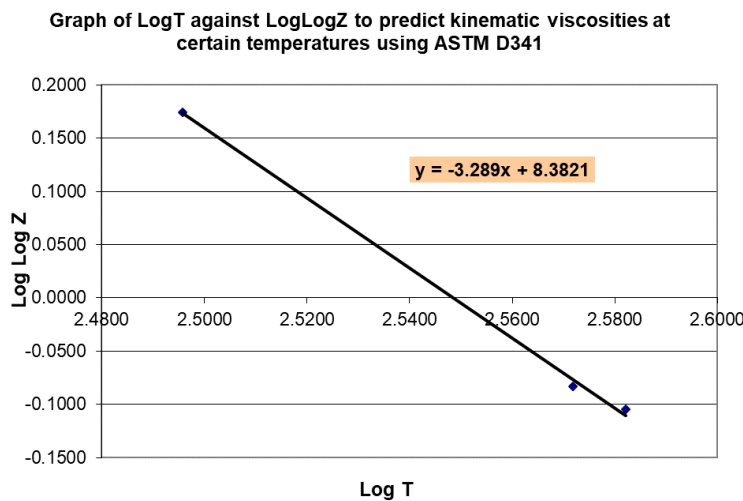

Figure 10-1 - Graph of LogT against LogLogZ to predict kinematic viscosities at certain temperatures using ASTM D341.

Consequently, the kinematic viscosity can be estimated at the test temperatures using ASTM D341 and these can be seen in Table 10-6.

Table 10-6 – The estimated kinematic viscosities using ASTM D341 of the base oils at the temperatures tested.

Ester description	Kinematic Viscosity cSt			
	60 °C	80 °C	100 °C	120 °C
PE with all n-C5 acid	8.48	5.29	3.92	2.65
PE with all n-C7 acid	11.40	6.95	4.66	3.36
PE with all n-C9 acid	15.65	9.33	6.14	4.35
TMP with all n-C7 acid	7.82	4.94	3.41	2.51
NGP with all n-C7 acid	3.61	2.54	1.91	1.52

The lubricants were also tested at the same viscosity by varying the test temperature for each base oil. These temperatures were also calculated using ASTM D341 and can be seen in Table 10-7.

Table 10-7 – Table showing the calculated temperatures at which, the base oils have the following viscosities.

Ester description	Temperature at which, the lubricant has a kinematic viscosity of (°C)		
	2.9 cSt	5 cSt	7.3 cSt
PE with all n-C5 acid	113.8	82.5	65.9
PE with all n-C7 acid	130.2	96.2	77.8
PE with all n-C9 acid	149	111.5	91.3
TMP with all n-C7 acid	110.1	79.4	62.7
NGP with all n-C7 acid	71.9	44.8	30

This same method was applied to the base oils using for the branching study and their calculated kinematic viscosities can be seen in Table 10-8 and Table 10-9.

Table 10-8 – The estimated kinematic viscosities for the base oils for the branching study using ASTM D341 of the base oils at the temperatures tested.

Ester description	Kinematic Viscosity cSt			
	60 °C	80 °C	100 °C	120 °C
MONOPE with all NC8	13.27	7.93	5.24	3.73
MONOPE with NC8: EH of 75:25	13.93	8.18	5.33	3.75

MONOPE with NC8: EH of 50:50	15.07	8.6	5.5	3.82
MONOPE with NC8: EH of 25:75	16.53	9.16	5.74	3.93
MONOPE with all NC8	19.32	10.26	6.24	4.18

Table 10-9 – Table showing the calculated temperatures at which, the base oils have the following viscosities.

Ester description	Temperature at which, the lubricant has a kinematic viscosity of (°C)		
	3 cSt	5 cSt	7cSt
MONOPE with all NC8	134.9	102.5	85.6
MONOPE with NC8: EH of 75:25	135.0	103.4	86.8
MONOPE with NC8: EH of 50:50	135.7	104.9	88.7
MONOPE with NC8: EH of 25:75	136.9	106.8	91.0
MONOPE with all NC8	140.1	110.5	95.0

This same method was applied to the fully formulated lubricants and their calculated kinematic viscosities can be seen in Table 10-10 and Table 10-11.

Table 10-10 - The estimated kinematic viscosities for the fully formulated lubricants using ASTM D341 at the temperatures tested.

Lubricant	Kinematic Viscosity cSt			
	60 °C	80 °C	100 °C	120 °C
Low	7.05	4.5	3.14	2.33
Medium Low	14.48	7.99	5.01	3.43
Medium High	22.31	11.65	6.99	4.63
High	27.15	13.79	8.1	5.28

Table 10-11 - Table showing the temperatures at which, the fully formulated lubricants have a kinematic viscosity of 5 cSt.

Oil	Temperature at which, the oil has a kinematic viscosity of 5 cSt (°C)
High	122.8
Medium High	115.9
Medium Low	100.6

Low	74.9

10.4 Calculation of the dynamic viscosities required for the Hersey Number

The density of these fluids was also required such that their dynamic viscosity could be calculated which, was needed to calculate the Hersey number. Whilst it is recognised that density varies with temperature; the densities could not be acquired for the different fluids at different temperatures. Hence, the room temperature density for each fluid was used for all calculations with the assumption that they densities remains different to each of the fluids. This method is only shown for the base oils in **Error! Reference source not found.** and the same method was used for all the other base oils in the study.

Table 10-12 –Densities pure base oils.

	NPG, all C7 acids	TMP, all C7 acids	PE, all C5 acids	PE, all C7 acids	PE, all C9 acids
Density of Liquids, 15.6 °C	0.9291	0.9628	1.022	0.9809	0.9569

The dynamic viscosity has been calculated from the density multiplied by the kinematic viscosities in Table 10-6 and then converted from cP to Pa. s by multiplying by 10^{-3}. These dynamic viscosities can be seen in Table 10-13. The density will change with temperature, but only the density at 15.6 °C could be acquired and hence, the dynamic viscosities have been estimated using this.

Table 10-13 – Dynamic viscosities at of the pure base oils at a range of temperatures.

Pa. s	Dynamic Viscosity Pa. s			
	60 °C	80 °C	100 °C	120 °C
NPG, all C7 acids	0.003354	0.00236	0.001775	0.001412
TMP, all C7 acids	0.007529	0.004756	0.003283	0.002417
PE, all C5 acids	0.008667	0.005406	0.004006	0.002708
PE, all C7 acids	0.011182	0.006817	0.004571	0.003296
PE, all C9 acids	0.014975	0.008928	0.005875	0.004163

Hence, the dynamic viscosities can also be calculated for when they were all tested at different temperature to achieve the same kinematic viscosity, these can be seen in Table 10-14.

Table 10-14 - Dynamic viscosities calculated from the kinematic viscosity.

Ester description	Dynamic viscosities calculated from the kinematic viscosity (Pa. s)		
	2.9 cSt	5 cSt	7.3 cSt

NPG, all C7 acids	0.00269439	0.0046455	0.0074606
TMP, all C7 acids	0.00279212	0.004814	0.00702844
PE, all C5 acids	0.0029638	0.00511	0.0074606
PE, all C7 acids	0.00284461	0.0049045	0.00716057
PE, all C9 acids	0.00277501	0.0047845	0.00698537

This same method was applied to the branched base oils and the densities and dynamic viscosity data can be seen in Table 10-15, Table 10-16 and

Table 10-17.

Table 10-15 –Densities pure base oils.

	MONOPE with all NC8	MONOPE with NC8: EH of 75:25	MONOPE with NC8: EH of 50:50	MONOPE with NC8: EH of 25:75	MONOPE with all EH
Density of Liquids, 15.6 °C	0.968	0.968	0.967	0.966	0.966

Table 10-16 – Dynamic viscosities at of the pure base oils at a range of temperatures.

Pa. s	Dynamic Viscosity Pa. s			
	60 °C	80 °C	100 °C	120 °C
MONOPE with all NC8	0.0128	0.0077	0.0051	0.0036
MONOPE with NC8: EH of 75:25	0.0135	0.0079	0.0052	0.0036
MONOPE with NC8: EH of 50:50	0.0146	0.0083	0.0053	0.0037
MONOPE with NC8: EH of 25:75	0.016	0.0088	0.0055	0.0038
MONOPE with all EH	0.0187	0.0099	0.006	0.004

Table 10-17 - Dynamic viscosities calculated from the kinematic viscosity.

Ester description	Dynamic viscosities calculated from the kinematic viscosity (Pa. s)		
	2.9 cSt	5 cSt	7.3 cSt
MONOPE with all NC8	0.0028072	0.00484	0.0070664
MONOPE with NC8: EH of 75:25	0.0028072	0.00484	0.0070664
MONOPE with NC8: EH of 50:50	0.0028043	0.004835	0.0070591

MONOPE with NC8: EH of 25:75	0.0028014	0.00483	0.0070518
MONOPE with all NC8	0.0028014	0.00483	0.0070518

This same method was applied to the fully formulated lubricants and the densities and dynamic viscosity data can be seen in Table 10-18, Table 10-19 and Table 10-20.

Table 10-18 –Densities of the fully formulated lubricants.

	Low	Medium Low	Medium High	High
Density of Liquids (specific gravity, unitless) 15.56 ℃	0.9669	0.9661	0.9677	0.9676

Table 10-19 – Dynamic viscosities at of the fully formulated lubricants at a range of temperatures.

Pa. s	Dynamic Viscosity Pa. s			
	60 °C	80 °C	100 °C	120 °C
Low	0.006816645	0.00435105	0.003036066	0.002252877
Medium Low	0.013989128	0.007719139	0.004840161	0.003313723
Medium High	0.021589387	0.011273705	0.006764223	0.004480451
High	0.02627034	0.013343204	0.00783756	0.005108928

Table 10-20 - Dynamic viscosities for the fully formulated lubricants calculated from the kinematic viscosity.

Lubricant Pa.s	Dynamic viscosities calculated from the kinematic viscosity (Pa. s)
	5 cSt
Low	0.00501531
Medium Low	0.004956093
Medium High	0.004858822
High	0.004872834

10.5 Estimation of the pressure viscosity coefficient at different test temperatures

The pressure viscosity coefficients (PVC) have also been supplied for these oils (Table 10-21) and have been used to calculate the film thickness and the therefore, the lambda ratio. This parameter also varies with temperature and the PVC at different temperatures has been estimated by plotting the known PVC against temperature and using the equation of the line to calculate the other temperatures. These can be seen in Table 10-22 and the graph of the plotted pressure viscosity coefficients can be seen in Figure 10-2. For most of the base oils, the PVC increases as temperature decreases except for TMP n-C7, this is not currently understood.

Table 10-21 – Supplied PVC of the pure base oils.

Pressure-Viscosity Coefficient, x 10^{-8} m²/N	NPG, all C7 acids	TMP, all C7 acids	PE, all C5 acids	PE, all C7 acids	PE, all C9 acids
at 40°C	0.67	1.07	2.28	2.18	0.92
at 70°C	0.63	1.13	1.57	1.49	0.72
at 100°C	0.6	1.18	1.21	1.13	0.6
at 130°C	0.58	1.22	0.99	0.92	0.52

Table 10-22 – Estimated pressure viscosity coefficients that have been calculated from the line equations in Figure 10-2.

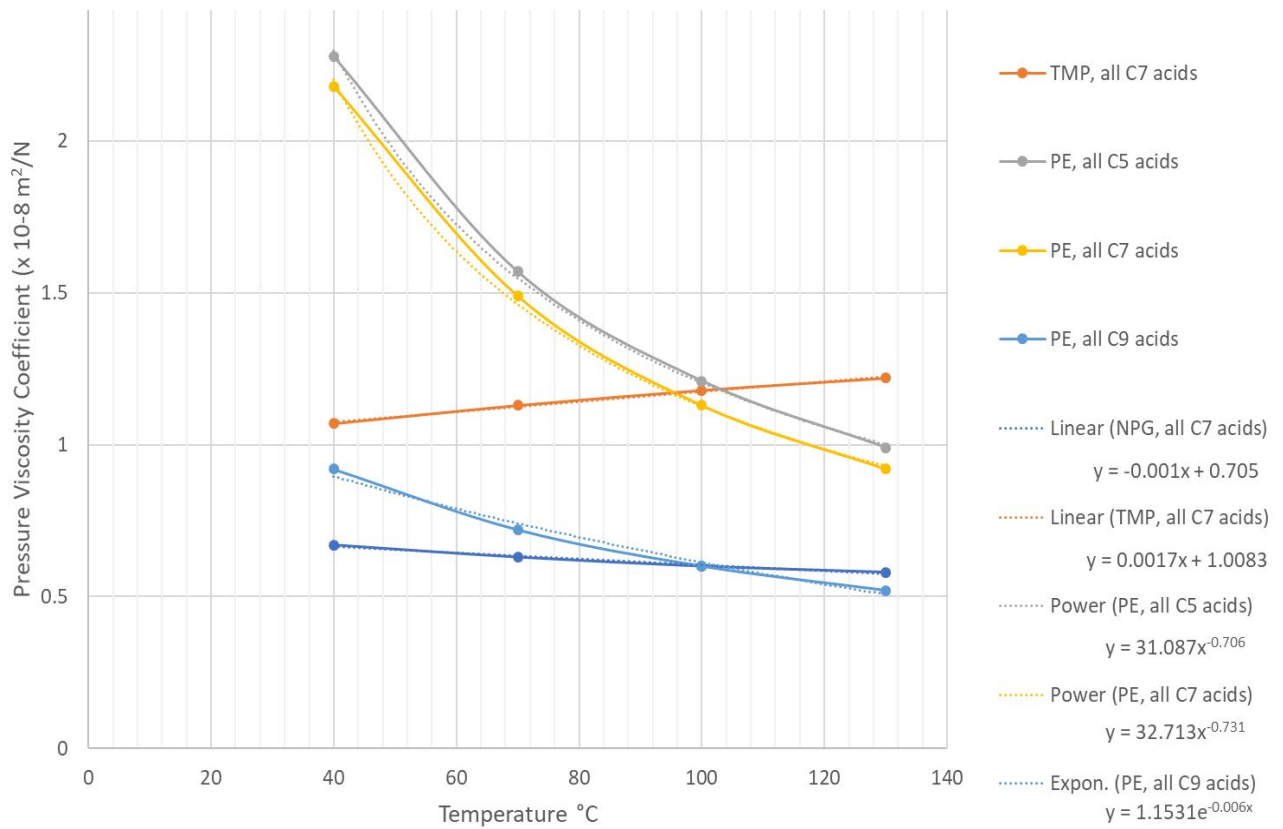| PVC estimation (based on line equations) x 10-8 m²/N	NPG, all C7 acids $y = -0.001x+0.705$	TMP, all C7 acids $y = 0.0017x+1.0083$	PE, all C5 acids $y = 31.087x^{-0.706}$	PE, all C7 acids $y = 32.713x^{-0.731}$	PE, all C9 acids $y = 1.1531e^{-0.006x}$
60	0.65	1.11	1.53	1.44	0.77
80	0.63	1.14	1.15	1.08	0.68
100	0.60	1.18	1.21	1.13	0.60
120	0.58	1.21	0.77	0.72	0.54
30	0.68				
44.8	0.66				
71.92	0.63				
62.7		1.11			
79.4		1.14			
110.1		1.19			
65.9			1.39		
82.8			1.11		
113.79			0.81		
77.8				1.11	
96.2				0.90	
130.2				0.66	
91.25					0.63
111.5					0.56
149					0.46

Figure 10-2 – Graph showing the pressure viscosity coefficients for the pure base oils plotted against the temperature. These were fit to line equations that allowed the estimation of the PVC at other temperatures.

The pressure-viscosity coefficients could not be acquired for the other base oils tested but is expected as they are more viscous fluids that they should all reach the EHD regime and the high entrainment speeds used during these tests on the MTM.

10.6 Base Oil Rheology

The base oils were tested using a Bohlin Gemini HR Nano Rotonetic Drive 2 rheometer with a cone on plate configuration. The parameters for the rheometer can be seen in Table 10-23. The cone attachment was a 40 mm stainless steel cone with a 4 ° angle. The tested conducted used a controlled shear stress ramp up to a shear rate of 200 s^{-1} and then back down to check for hysteresis. Temperature was controlled using the Peltier plate attachment.
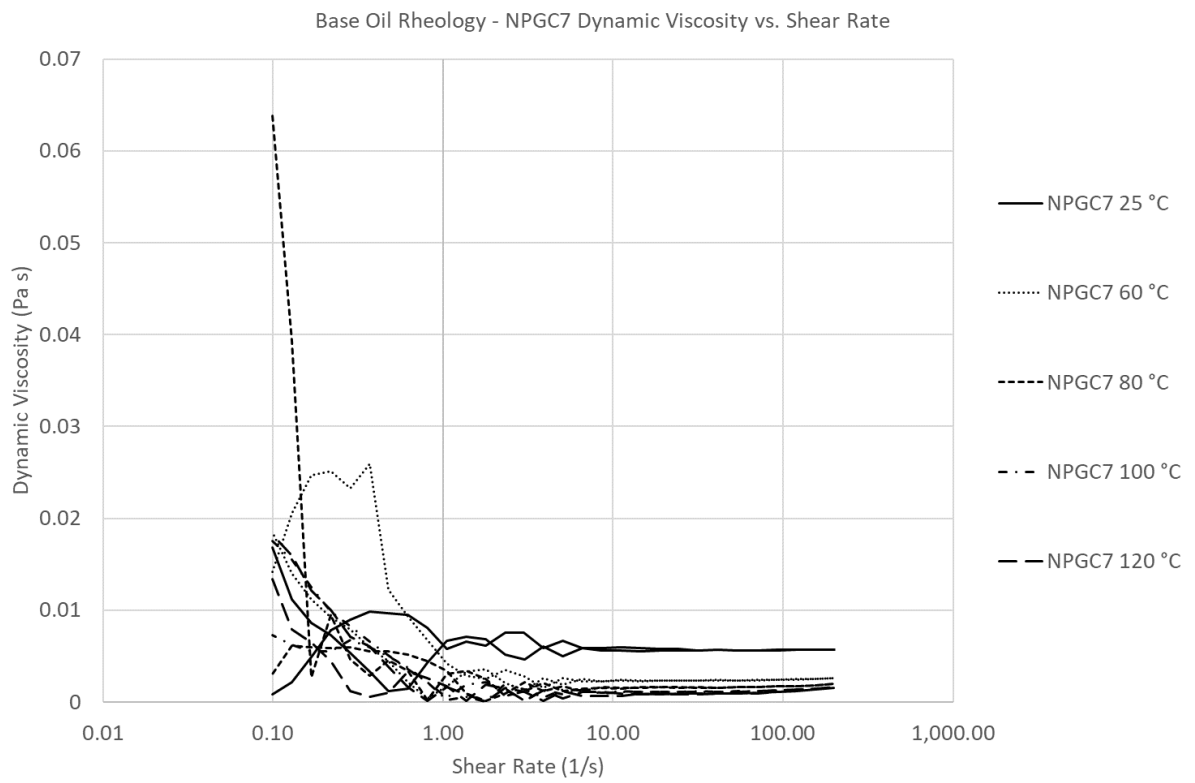
All the base oils were tested at 25 °C but only 2 of the base oils were tested at a range of temperatures to show to show that there is no effect with temperature and viscosity influencing non-Newtonian behaviour. The base oils tested were the NPG C7 base oil shown in **Error! Reference source not found.** and the "High" formulated lubricant. The rationale was that if these were Newtonian, the base oils in between this viscosity range with a similar chemistry are also Newtonian.

Table 10-23 – Table showing the parameters for the Bohlin Gemini HR Nano Rotonetic Drive 2 rheometer.

Parameter	Value
Torque Range in controlled stress & rate viscometry:	10nNm to 200mNm
Torque Range in controlled stress & strain oscillation:	3nNm to 200mNm
Torque resolution:	Better than 1nNm
Position resolution:	50nrad
Frequency range:	1µHz to 150Hz
Controlled speed range (CR mode):	0.01mrad s-1 to 600rad s-1
Measurable speed range (CS mode):	10nrad s-1 to 600rad s-1
Normal force N1 measurement range:	0.001N to 20N (50N optional)
Step change in strain:	<10ms
Temperature controls: Peltier Plate:	-30ºC to 200ºC
Nominal operating voltage	110 or 220V
Size (with Peltier plate)	52cm (H) x 33cm (W) x 37cm (D)
Weight (with Peltier plate)	28kg

It can be seen from Figure 10-3 and Figure 10-4 that the lowest and highest viscosity lubricants in this study are Newtonian and therefore, all the base oils used in this study can be assumed to be Newtonian. The graphs are expected to be noisier at lower speeds and more so with less viscous fluids

however, it can be seen at higher shear rates, the viscosity remains relatively constant with shear thus suggesting Newtonian behaviour.

Base Oil Rheology - NPGC7 Dynamic Viscosity vs. Shear Rate

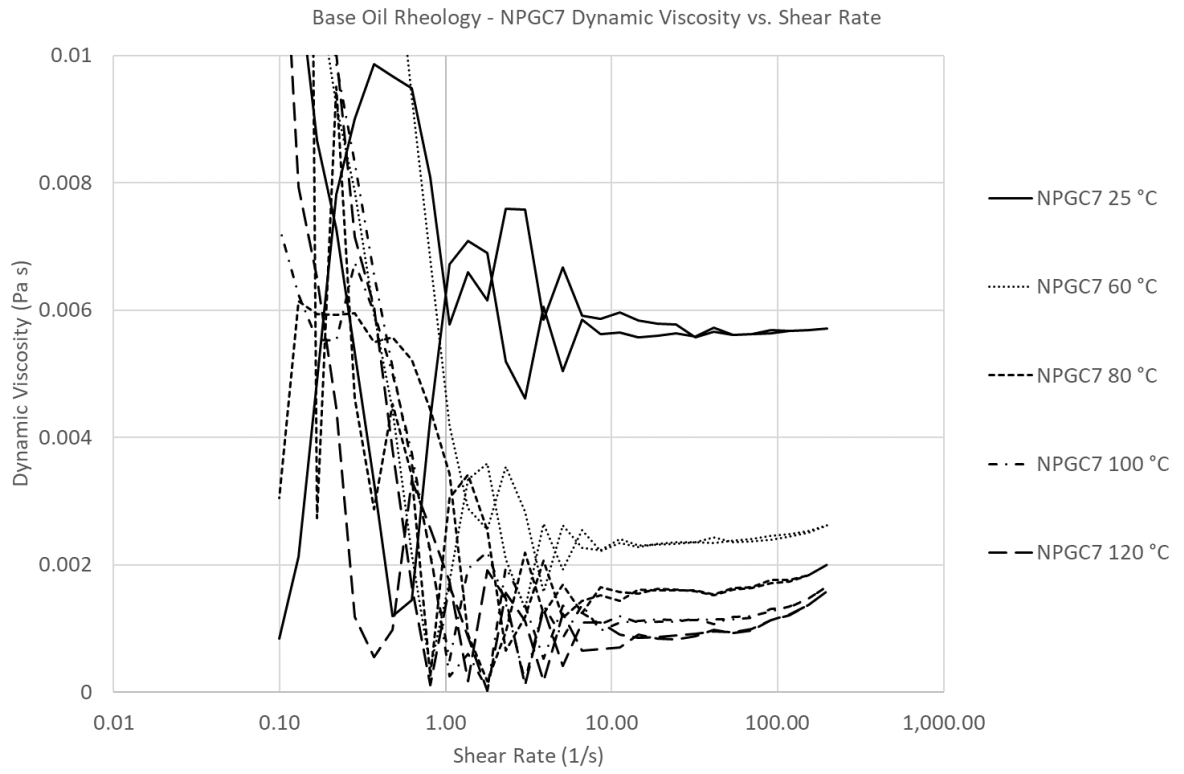Base Oil Rheology - NPGC7 Dynamic Viscosity vs. Shear Rate

Figure 10-3 – Graph showing the measured dynamic viscosity against shear rate for NPGC7 showing Newtonian behaviour.
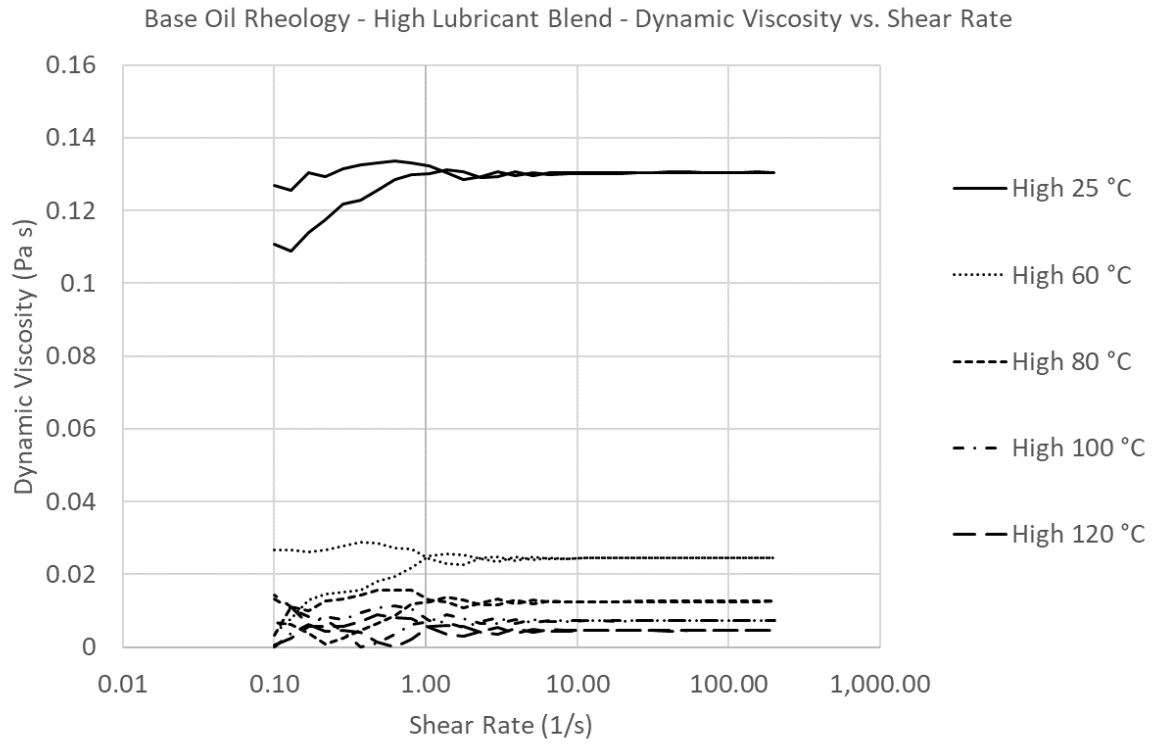
Figure 10-4 – Graph showing the measured dynamic viscosity against shear rate for the High lubricant blend showing Newtonian behaviour.